Investigation of frustrated magnetism in double perovskites

INVESTIGATION OF FRUSTRATED MAGNETISM IN DOUBLE PEROVSKITES

By

CASEY ANN MARJERRISON, B.A.SC.

A Thesis
Submitted to the School of Graduate Studies
in Partial Fulfilment of the Requirements
for the Degree
Master of Science

McMaster University

Master of Science (2016) McMaster University

(Department of Physics and Astronomy) Hamilton, Ontario

TITLE: Investigation of frustrated magnetism in double perovskites

AUTHOR: Casey Marjerrison, B.A.Sc.

SUPERVISOR: Bruce D. Gaulin

NUMBER OF PAGES: xvi, 88

Abstract

This investigation studies the structural and magnetic properties of the double perovskites Ba_2YRuO_6, Ba_2YReO_6,Ba_2YOsO_6, Ba_2MgReO_6, Ba_2ZnReO_6, $Ba_2Y_{2/3}ReO_6$, Ba_2MgOsO_6, Ba_2ZnOsO_6, Ba_2CdOsO_6, La_2LiRuO_6, and La_2LiOsO_6. These compounds were prepared as powders using conventional solid state techniques. Structural characterization was performed with room temperature powder x-ray diffraction, and for most compounds, room temperature and low temperature powder neutron diffraction. The double perovskites in this investigation can be categorized as cubic Fm-3m and monoclinic $P2_1/n$. Over the ranges of temperatures measured, no space group changes were detected. Magnetic susceptibilty, magnetic hysteresis, and heat capacity measurements revealed a variation of ground states and magnetism across this selection of double perovskites. Inelastic neutron scattering experiments gave evidence for spin gap formation in almost all of the compounds.

Acknowledgements

I would like to sincerely thank my supervisor Dr. Bruce Gaulin for allowing me the opportunity to be his student. Bruce was always very encouraging, patient, and easy to approach. He creates thoughtful projects which caters to each of his student's strengths in order for them to grow to their fullest potential. It is hard to imagine another supervisor who could have provided as much for me as Bruce and I can never thank him enough for this.

Hanna Dabkowska, Antoni Dabkowski, John Greedan, Tim Munsie, Corey Thompson, and Yurij Mozharivskyj you are some of the most influential people in my entire life. Without your guidance, endless patience, and enthusiasm there is no absolutely no way I would have ever made it this far. You have each taken it upon yourselves to instil even some fraction of your knowledge and expertise in me and for that I am eternally grateful. I consider all of you to be like family for me and I'm certain that if it wasn't for all the lunchtime fruit over the years I would probably have gotten scurvy at some point.

Bruce's research team shares his enthusiasm, patience, and easy to approach nature. I would like to thank the following labmates who taught me so much, went on experiments with me, gave me helpful insights, and took a personal interest in my life: Jonathan Gaudet, Connor Buhariwalla, Dalini Maharaj, Gabriele Sala, Jerod Wagman.

Behind all the hardships and struggles my family and friends have always supported to me. My amazing mother, father, and brother - Shelley, Michael, and Gregory Marjerrison - have always provided comfort, encouragement, and inspiration whenever I felt like giving up. My friends have always been there to support me in and outside the laboratory.

Co-Authorship

I would like to formally acknowledge the contributions, assistance, and technical support from the following scientists and collaborators. Dr. John Greedan and Dr. Corey Thompson were instrumental in a number of ways: the development of synthesis procedures, x-ray and neutron diffraction Rietveld refinements and experiments, taking physical property measurements, solving magnetic structures and magnetic data, fitting heat capacity data, preparation of manuscripts and presentations. Dr. Paul Dube was extremely useful and reliable in the operation of the SQUID magnetometer and the Oxford property measurement system. Arzoo Sharma and Dr. Chris Wiebe from the University of Winnipeg performed numerous heat capacity measurements and magnetic measurements. The neutron instrument scientists Dr. Roxana Flacau from Chalk River National Laboratories and Dr. Garrett Granroth from Oak Ridge National Laboratories were knowledgeable and eager to assist. Several members of Bruce Gaulin's research team, Dalini Maharaj, Gabriele Sala, Edwin Kermarrec, J.P. Carlo, and Pat Clancy performed neutron scattering experiments on the samples.

List of publications involved in this investigation with contributions:

"Spin gap and the nature of the 4d3 magnetic ground state in the frustrated fcc antiferromagnet Ba2YRuO6". Physical Review B: Condensed Matter and Materials Physics (2013), 88(2)-*synthesis, x-ray diffraction, magnetic measurements, participation at neutron experiment on the SEQUIOA beamline*

”Frustrated fcc antiferromagnet Ba2YOsO6: structural characterization, magnetic properties, and neutron scattering studies”. Physical Review B: Condensed Matter and Materials Physics (2015), 91(7)-*synthesis, x-ray diffraction, magnetic measurements, participation at neutron experiment on the C2 beamline*

”Cubic Re6+ (5d1) Double Perovskites, Ba2MgReO6, Ba2ZnReO6 and Ba2Y2/3ReO6.Magnetism, Heat Capacity, SR , Neutron Scattering Studies and Comparison with Theory”. In submission-*synthesis, x-ray diffraction, magnetic measurements, heat capacity measurements, participation at neutron experiment on the C2 beamline*

”Frustrated magnetism in the double perovskite La2LiOsO6: A comparison with La2LiRuO6”. Physical Review B: Condensed Matter and Materials Physics (2016), 93(1)-*synthesis, x-ray diffraction, magnetic measurements*

Table of Contents

List of Figures

List of Tables

Chapter 1

Introduction

1.1 Transition and rare earth metal oxides

Transition metal and rare earth oxides display a wide variety of physical properties such as magnetism, superconductivity, and thermoelectricity to mention a few. Focusing on the topic of magnetism, there are a number of factors which contribute to magnetic ordering and its origin. Transition metal and rare earth oxides typically form a periodic three dimensional array referred to as a crystal lattice, due to the largely ionic nature of the chemical bonds[6]. These crystal lattices provide a symmetry driven framework in which to investigate the mechanisms of magnetic ordering. Due to the high amount of symmetry and concentration of magnetic ions, long-range magnetic order, typically due to superexchange interactions, can occur. Superexchange interactions, where magnetic moments are coupled to one another due to orbital overlap via an intervening diamagnetic ligand such as O^{2-} and the Pauli exclusion principle, are quantified by the exchange constant J[6]. This constant can be determined experimentally and is then used to determine the underlying magnetism and its origin.

One type of symmetry to consider is the arrangement of oxygen atoms relative to the metal atoms. The number of oxygen atoms around a metal centre is called the coordination number and their geometry influences the valence electrons on the metal centre. The oxygen is present in the compound as O^{2-} and for simplicity can be viewed as a region of negative charge. For transition metals the valence electrons on the metal centres are contained in the d orbitals. Orbitals which are pointing directly towards O^{2-} ions will experience greater charge repulsion than orbitals which are not pointing towards O^{2-} ions. This causes a splitting in the degeneracy of the energy levels of the orbitals.

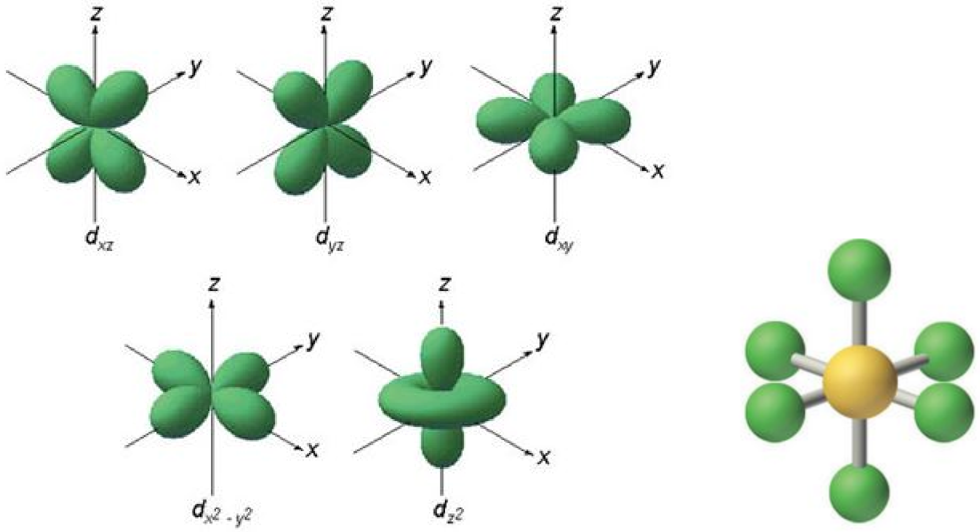

Figure 1.1: Schematic of 3d orbitals and octahedral oxygen environment

Consider the 3d orbitals in an octahedral environment of oxygen ions as shown in Figure 1.1. The $3\mathrm{d}_{x2-y2}$ and $3\mathrm{d}_{z2}$ orbitals will be raised in energy to form a degenerate set of orbitals called the e_g orbitals. The $3d_{xy}$, $3d_{xz}$, and $3d_{yz}$ orbitals will be lowered in energy to form a degenerate set of orbitals called the t_{2g} orbitals as shown in Figure 1.2. An understanding of orbital degeneracy allows for a qualitative assessment of physical properties and can provide a physical basis for phenomena such as Jahn-Teller distortions which can bring about a structural change in the crystal lattice.

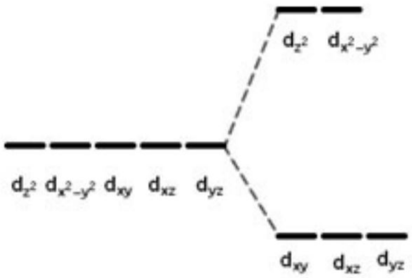

Figure 1.2: Schematic of splitting 3d orbitals into two degenerate energies

The high temperature random magnetic state is referred to as paramagnetism. The moments will align to an applied magnetic field but will lose this alignment when the magnetic field is no longer being applied. In an ordered magnetic state, there exists long range correlations between the magnetic moments. In all magnetic materials there is a coupling of moments between magnetic ions which can be described with a Hamiltonian. This Hamiltonian typically includes terms such as nearest neighbours interactions and next nearest neighbours interactions[7]. Depending on the number of terms used in the Hamiltonian, the crystallography, and the number of magnetic ions, this coupling ranges in complexity with a simple case being ferromagnetism using an Ising type model. The Ising model assumes only one spin degree of freedom where spins can be aligned parallel or antiparallel to a particular axis[7]. In measurements this is seen as slightly perturbed paramagnetic behaviour until the critical temperature T_C is reached. At this temperature the moments become aligned parallel to the applied magnetic field as shown in Figure 1.3. The sample remains magnetized even after the field is no longer being applied. Another type of magnetism is antiferromagnetism. In measurements this is seen as slightly perturbed paramagnetic behaviour until the critical temperature T_N is reached. At this temperature the moments become aligned antiparallel to the applied magnetic field as shown in Figure 1.3.

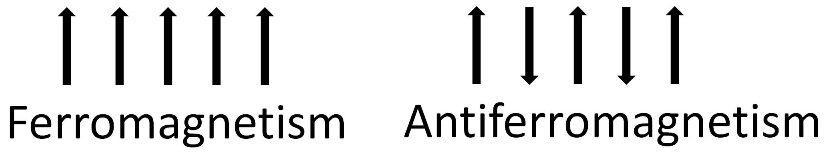

Figure 1.3: one dimensional schematic of ferromagnetic and antiferromagnetic ordering

These simple cases shown in Figure 1.3 use an Ising type model and do not display the more complex geometries and magnetic interactions which are available in two or three dimensional cases. Consider antiferromagnetic interactions on the equilateral triangular lattice shown in Figure 1.4. There is no arrangement of spins such that they are all simultaneously antiparallel to their nearest neighbours, leading to geometric frustration. This occurs in a series of two and three dimensional triangular, hexagonal and tetrahedral geometries. This geometric frustration leads to an entropy dominated system even at low temperatures and can give valuable insights into hypothetical phenomena such as a spin liquid state at zero Kelvin.

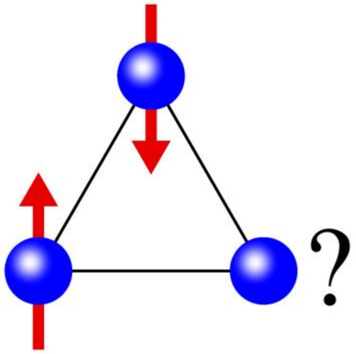

Figure 1.4: Geometric frustration due to nearest neighbour antiferromagnetic coupling on an equilateral triangular.

1.2 Double Perovskites

Perovskite materials are a family of compounds which all have the chemical formula ABX_3. For transition metal oxides, the X site is typically oxygen though some site substitutions with fluorine or nitrogen are reported, the A site is often a large alkali or alkaline earth metal (the lanthanide atoms and actinides are also a possibility) and the B site is commonly a transition metal. This large variability in the A site and B site alone allows for a wide range of possible compounds that can be formed and studied. In the case of double perovskites, one can imagine taking two perovskites with the form ABX_3 and $A'B'X_3$ and combining them to form a double perovskite of the form $AA'BB'X_6$. Note that double perovskite compounds are not simply mixtures of two perovskites with domains and grain boundaries between the two types but an overarching lattice structure. Depending on the ionic radii and charge of the A and A′

ions, these sites can be mixed if the ionic radii and charge of the A and A′ ions are similar. For many transition metal oxide double perovskites this tends to be the case. In case of the double perovskites presented in this thesis, the A ion and A′ ion are identical. Similarly for the B and B′ site, depending on the ionic radii and charge of the B and B′ ions, these sites can also be mixed if the ionic radii and charge of the B and B′ ions are similar. For the purpose of investigating magnetism in geometrically frustrated arrangements, it's desirable to have only one magnetic site which is fully occupied by only one species of ion and the rest of the ions and sites to be non-magnetic. This can be achieved by selecting pairs of B and B′ ions such that the difference between their ionic radii and formal oxidation state is very large[8]. These pairs are also chosen such that one of the ions has a closed valence shell configuration (and is thus nonmagnetic) and the other ion has a desired number of valence electrons. The ionic radii of the 4d transition metals in similar to that of the 5d transition metals which allows for investigations which also probe the effects of differences in 4d and 5d orbitals and spin-orbit coupling without changing the geometric arrangement of the ions substantially or the number of valence electrons on the magnetic site if desired. Pairs which have a charge difference of at least two tend to form charge ordered sites with site mixing on the order of one percent or less. The ionic radii of the A,A′,B,B′, and X ion can also be used to determine the overall crystal structure the double perovskite is most likely to form. A number called the tolerance factor, t, can be calculated in the following manner[8]:

$$t = \frac{\frac{r_A}{2} + \frac{r_{A'}}{2} + r_X}{\sqrt{2}(\frac{r_B}{2} + \frac{r_{B'}}{2} + r_X)}$$

This definition for the tolerance factor is arranged to be exactly one for a cubic system. The greater the deviation from unity, the less crystal symmetry the lattice will have. For perovskites the tolerance factor typically falls in the range of $\sim 0.9 \leq$ t ≤ 1.0 with space group symmetry ranging from $P2_1/n \leftarrow I4/m \leftarrow Fm\text{-}3m$. In this investigation, cubic and monoclinic crystal lattices were studied.

The cubic lattice forms into the space group Fm-3m with a representative atomic arrangement shown in Figure 1.5. When performing crystal structure refinements on the cubic system, the following atomic positions were used (as shown in Table 1.1) and the thermal factor, B, was refined to be a non-negative value of a reasonable magnitude.

Ion	Site	Occupancy
A,A′	(0.25,0.25,0.25)	1.0
B	(0.5,0.5,0.5)	1.0
B′	(0,0,0)	1.0
X	(0.25-δ,0,0)	1.0

Table 1.1: Atomic positions for a cubic double perovskite.

The magnetic sublattice formed by considering only the B′ site is shown in Figure 1.6. The bond distances between nearest neighbour B′ ions are identi-

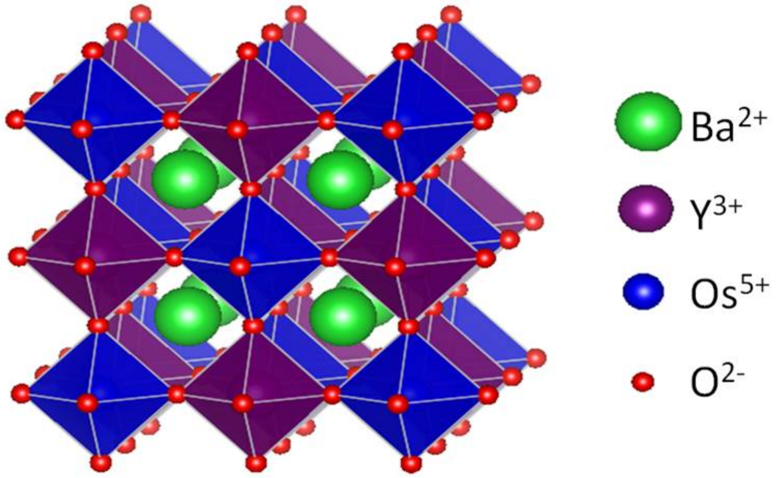

Figure 1.5: Crystal lattice of cubic Fm-3m Ba_2YOsO_6 with colour legend

cal,which forms a network of edge sharing tetrahedra. This geometric arrangement can lead to a large degree of geometric magnetic frustration.

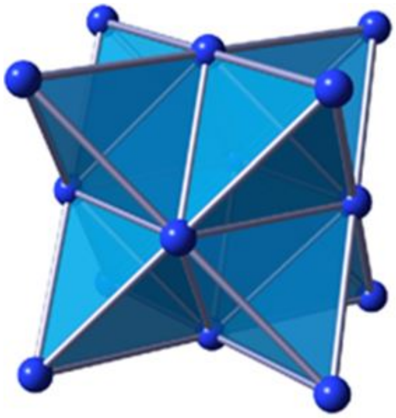

Figure 1.6: Magnetic sublattice of cubic double perovskites

The monoclinic lattice forms into the space group $P2_1/n$ with a representative atomic arrangement shown in Figure 1.7. When performing crystal structure refinements on the monoclinic system, Table 1.2 shows the atomic positions used for La_2LiOsO_6 which were taken from previous literature[9](for

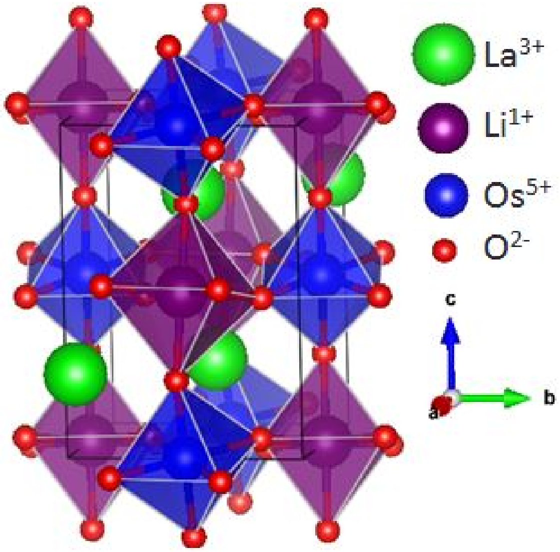

Figure 1.7: Crystal lattice of monoclinic $P2_1/n$ La_2LiOsO_6 with colour legend

the ruthenium based compound [4]) and the thermal factor, B, was refined to be a non-negative value of a reasonable magnitude.

Ion	Site	Occupancy
A,A′	(0.49116,0.04600,0.25114)	1.0
B	(0,0,0)	1.0
B′	(0.5,0.5,0)	1.0
X1	(0.21820,0.30110,0.04150)	1.0
X2	(0.57880,0.48280,0.24180)	1.0
X3	(0.30320,0.78180,0.04370)	1.0

Table 1.2: Atomic positions for monoclinic double perovskite La_2LiOsO_6.

The magnetic sublattice formed by considering only the B′ site is shown in Figure 1.8. The nearest neighbour B′ ions still form a network of edge sharing tetrahedra but the bond distances are not quite identical as in the case of the cubic system. This will still lead to a degree of geometric magnetic frus-

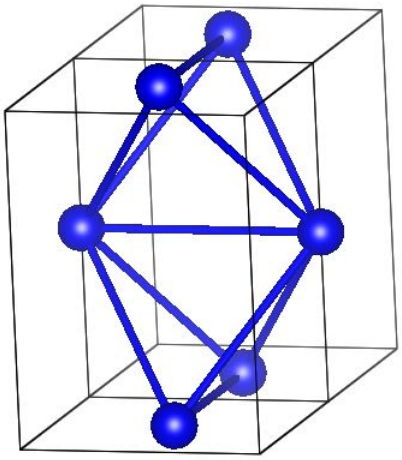

Figure 1.8: Magnetic sublattice of monoclinic double perovskites

tration but the monoclinic system will not be as frustrated as the cubic system.

Chapter 2

Experimental Techniques

2.1 Solid state reactions

Solid state reactions of metals, metal oxides and metal carbonates are used to produce a large variety of materials. These materials can take on many different types of symmetries and properties. Site substitution of one element for another allows for an indepth investigation of properties such as magnetism to be explored experimentally with macroscopic approaches. Complicated effects such as spin orbit coupling in 5d metals compared to their 4d and 3d metals congeners can be observed through site substitution and magnetic measurements. The procedure of combining metals, metal oxides and metal carbonates then subjecting them to heat, atmosphere and pressure in order to produce a pure material of a desired composition is a non-trivial matter. Typically temperatures on the order of 1000^{O}C are used with time scales on the order of hours or days. The crucibles used in these reactions must also be able to withstand these high temperatures, rapid changes in temperatures and not undergo any reactions with the precursors or final product. Particle size, precursor homogeneity and overall sample size all influence the formation of the final product. Regrindings between subsequent mixtures improves homogeneity as well as particle size. It should be also be noted that not all phases are equilibrium stable phases and can be metastable states. In these circumstances a temperature quench may be required. Some precursors may also evaporate, resulting in an off-stoichiometric mixture if not accounted for correctly.

2.2 X-Ray diffraction

X-ray diffraction includes a range of techniques which can be used to determine the structure of materials and derive the orientation single crystals. Diffraction experiments map out the reciprocal lattice of a crystalline material by measuring the intensity of scattered X-rays as a function of the detector position relative to the X-ray source. If an incoming X-ray has wave vector $\vec{k}$ and scatters to $\vec{k}'$, it has a scattering vector of $\Delta\vec{k}$=$\vec{k}$-$\vec{k}'$. Scattering can only occur when $\Delta\vec{k}$ is equal to an integer multiple of the reciprocal lattice vector $\vec{a}$: $\Delta\vec{k}$=n$\vec{a}$ [10]. This is an extension of Bragg's Law: nλ=2dsinθ where n is the order of the diffraction, λ is the X-ray wavelength, d is related to the interplanar spacing in the crystal lattice and θ is the dispersion angle[10]. For powder X-ray diffraction (XRD), a collimated monochromatic X-ray source with a rotating sample stage and a detector with a θ degree of freedom are used. The X-ray source is a copper anode which produces Kα_1, Kα_2, and Kβ radiation. In order to produce a monochromated beam with only Kα_1= 1.541 $\mathring{A}$, a nickel filter is used to absorb the Kβ radiation and a germanium crystal monochromator is used to exclude the Kα_2 radiation. The sample stage contains a goniometer which spins the sample so that all the different planes of orientation are measured. The θ angle of the X-ray source remains fixed and the X-ray detector rotates relative to the stage which are given as 2θ angles by convention as shown in Figure 2.1. The detector rotates through a range of angles and measures the intensity of the X-rays. Angular positions with a large diffracted intensity reveal structural information and the spacing of atoms in the crystal lattice. These data are analyzed and compared to known structures using databases such as EVA and subsequently fit to a structural model using the Rietveld refinement program[11].

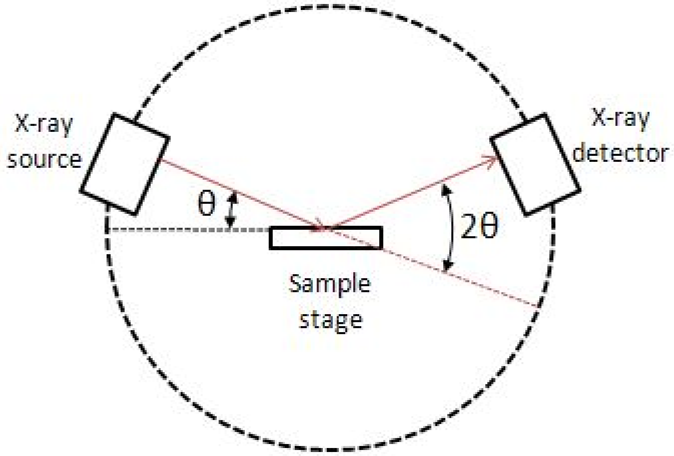

Figure 2.1: Schematic of X-ray diffraction experimental setup for powder X-ray diffraction

2.3 Magnetization by SQUID magnetometry

A superconducting quantum interference device (SQUID) magnetometer combines the flux quantization phenomenon and Josephson tunnelling to measure extremely small magnetic fluxes with very high precision [12]. The flux inside a superconducting ring is quantized by[10]:

$$\Phi = \frac{nh}{2e}$$

where n is an integer, h is Planck's constant and e is the charge of the electron. SQUID magnetometry allows you to measure the magnetization of a sample over a range of temperatures and applied magnetic fields. When measuring a sample there are two main modes which will be considered. Zero field cooling (ZFC) involves cooling the sample with no magnetic field applied and then applying the magnetic field for measuring after the sample has reached temperature. Field cooling (FC) involves cooling the sample with the magnetic field applied and then measuring the sample when it reaches temperature. Differences between the ZFC and FC measurements indicate that the magnetization is not a property of thermal equilibrium as it is path dependent.

Paramagnetism provides a magnetic susceptibility profile comparable to the one shown in Figure 2.2. At higher temperatures, thermal fluctuations keeps the spins from aligning parallel to the applied field. As the temperature decreases a larger component of the spins align parallel to the applied field. This can also occur at significantly large magnitudes of applied fields. This behaviour is described in the relation called the Curie Law[10]:

$$\chi = \frac{M}{H} = \frac{C}{T}$$

where χ represents the magnetic susceptibility, M is the magnetization, H is the applied field, T is the temperature and C is the Curie constant.

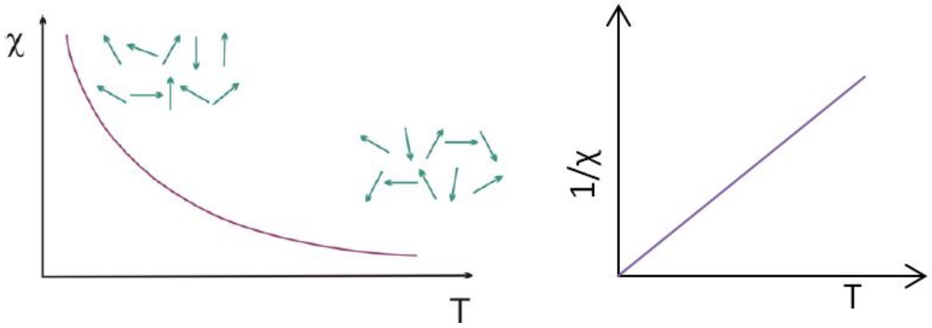

Figure 2.2: Example representations of the magnetic susceptibility and inverse susceptibility in paramagnetism, C=1/slope of the inverse susceptibility

Ferromagnetism provides a magnetic susceptibility profile comparable to the one shown in Figure 2.3. At a critical temperature referred to as T_c the Curie temperature, the spins align parallel to the field. This behaviour resembles paramagnetism however all the spins align completely and the x-intercept of the inverse susceptibility is a positive value instead of zero as it is in paramagnetism.

Antiferromagnetism provides a magnetic susceptibility profile comparable to the one shown in Figure 2.4. At a critical temperature referred to as T_N the Neel temperature, the spins align antiparallel to their nearest neighbouring spins[10]. This behaviour can be described by a modification to the Curie law used for paramagnetism called the Curie-Weiss law[10]:

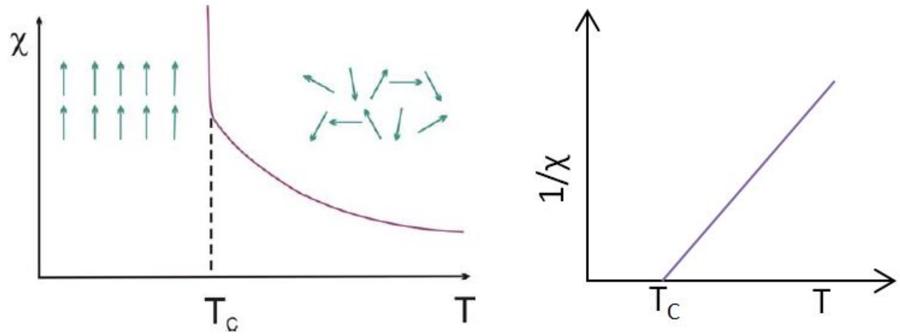

Figure 2.3: Example representations of magnetic susceptibility and inverse susceptibility in ferromagnetism

$$\chi = \frac{C}{T - \theta}$$

where C is the Curie constant and θ is the Weiss constant. The strength of the spin-spin interactions can be determined by fitting this line to the straight line region of the inverse susceptibility, which resembles a paramagnetic region, to determine the Weiss constant[10]. This Weiss constant will be a negative value and the more negative it is, the greater the strength of the antiferromagnetic interactions. This comparison is only valid when comparing compounds with the same spin value and crystal structures because θ depends on the spin value and the number of nearest neighbours and next neighbours etc. A positive Weiss constant corresponds to ferromagnetic correlations.

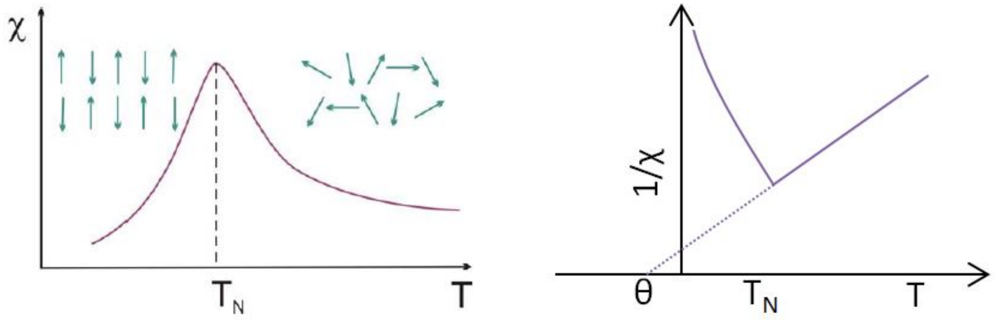

Figure 2.4: Example representations of magnetic susceptibility and inverse susceptibility in antiferromagnetism

From the Curie constant C, which is taken as the slope of the inverse susceptibility plot in a linear high temperature, an effective moment can be extracted by using[10]:

$$\mu = \sqrt{8C}\mu_B$$

Another application of SQUID magnetometry is to measure magnetic hysteresis in a sample. This is done by first cooling the temperature below the magnetic ordered state, typically to base temperature, then applying a strong negative magnetic field and sweeping through zero magnetic field to a strong positive magnetic field and then reversing from strong positive field to strong negative field. This measurement is performed on ferromagnetic materials to assess whether the material can be classified as a hard or soft magnet. Shown on the left in Figure 2.5, is a hard magnet which displays a large variance between the paths and on the right is a soft magnet which displays almost no path dependence[12]. If the applied field is sufficiently large it can also indicate the saturated moment of the material when all of its moments are pointed along the direction of the applied field.

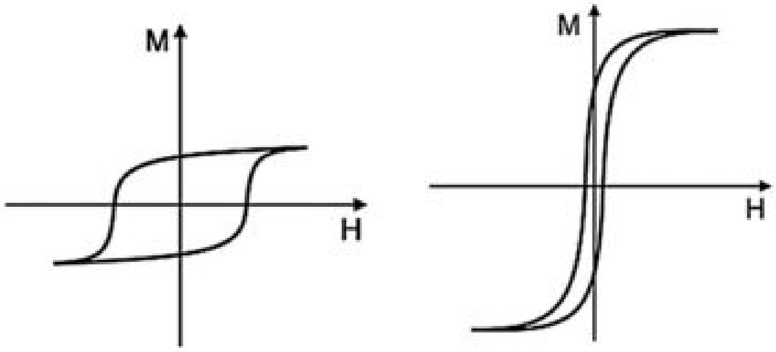

Figure 2.5: Example representations of magnetic hysteresis for a hard magnet on the left and a soft magnet on the right

2.4 Heat capacity

Heat capacity measurements were performed using the Oxford Instruments Maglab system using the quasi-static equilibrium relaxation method [13]. For these measurements 10 mg sintered pellets were fixed on a sapphire plate with 100 ug of apezion grease and heat pulses were applied. The contribution from the apezion grease was subtracted from the final results. By applying a known amount of heat to the system, knowing the sample mass and the mass of the apezion grease then waiting for the system to release the heat (relaxation) it is possible to determine the heat capacity. Sharp features such as lambda anomalies[13] indicate phase transitions in the material. For example these phase transitions can be structural or magnetic. One method for confirming if a peak is potentially magnetic in origin is to measure the heat capacity of an isostructural compound with no magnetic sites and compare. This technique is complemented by low temperature x-ray or neutron diffraction, high temperature x-ray or neutron diffraction and magnetic susceptibility. Typically, if there is no structural change observed by diffraction and the transition temperature in the magnetic susceptibility data matches the temperature at which a feature is observed in the heat capacity and that is high likely to be magnetic in origin. If the isostructural compound closely matches the lattice parameters and atoms in the desired compound then it can be considered as a reasonable match for the lattice contributions to the heat capacity. The lattice contributions can often be fitted to a power law involving odd powers of T^n, with n=1,3,5[7]. The materials studied in this investigation are all assumed to be insulators.

2.5 Neutron scattering

Neutrons are a unique probe of matter since they are electrically neutral Fermions with a magnetic moment of $1.91304272(45)\mu_N$, where $\mu_N = \frac{e\hbar}{2m_p}$[14],and thus interact weakly with matter. This allows for bulk structural and magnetic investigations of materials without damaging the sample or altering the fundamental physics taking place. Additionally, neutrons are able to produce or destroy low energy excitations in materials, such as phonons and magnons, by losing or gaining energy from the sample. However, since neutrons are electrically neutral, relatively low in energy, and in flux compared to x-ray scattering, a large number of neutrons is required in order to perform measurements. Neutron scattering uses a beam of neutrons produced by either a neutron fission reactor or a neutron spallation source. In the case of a fission reactor, a continuous flow of neutrons is produced from a radioactive source such as uranium. Spallation sources use heavy metal targets (large atomic number Z and correspondingly a large number of neutrons, mercury for example) that are bombarded by pulses of protons which are produced in an accelerator ring. When the target is hit by the proton pulses it releases neutron pulses. Spallation sources produce neutron pulses and flux reactors produce a continuous flow of neutrons. These different approaches to neutron production allow for different experimental designs to utilize the neutrons produced. Since neutrons are able to lose or gain energy by interacting with the sample, neutron scattering is often broken into two categories, elastic neutron diffraction and inelastic neutron scattering.

Elastic neutron diffraction refers to neutron scattering where the neutron maintains the same incident energy and does not gain or lose energy to the sample. The neutrons are typically viewed as matter waves in this type of experiment, hence elastic neutron diffraction. This technique works very similar to the x-ray diffraction discussed earlier with the addition that the neutron is also able to scatter off of magnetic moments as well. However, unlike x-rays which scatter off of electron cloud densities and thus more electrons (higher atomic number Z) equals greater scattering, neutrons scatter due to interaction with the nucleus itself and the magnetic moments on the atom. Each atom has a characteristic neutron scattering cross length, b, which is independent of its atomic number. This can be extremely useful in determining atomic structures which contain low atomic number atoms or atoms that are close in atomic number that are difficult to either detect or distinguish with a conventional technique such as x-ray diffraction. Neutrons are also capable of determining long range magnetic structures. Magnetic structures can have different symmetry and periodicity from the underlying atomic structure. For a simple example, consider a one dimensional chain of monoatomic atoms which are spaced a distance, D, apart as shown in Figure 2.6.

Figure 2.6: Illustration of antiferromagnetic ordering in a one dimensional monoatomic basis which has double the unit cell parameter of the atomic unit cell.

Beside the monoatomic chain of atoms in Figure 2.6 is that exact chain but with antiferromagnetically aligned moments. The atomic structure has a unit cell length of D but the magnetic structure would have a unit cell length of 2D. Since the magnetic structure does not have the same unit cell as the atomic structure, a different set of diffraction peaks will be generated when the system is in a magnetically long range ordered state. Another simple example is to consider the same one dimensional chain of monoatomic atoms except this time the spins are all ferromagnetically aligned and pointing in the same direction. In this case the atomic and magnetic unit cell length will be D and therefore both the atomic and magnetic diffraction peaks will occur at the same scattering angles. It is important to note that these two simple one dimensional models do not describe more complex systems that occur in real material systems. The two one dimensional cases assumed that the periodicity of the magnetic moments had to be commensurate (integer value multiple) with the atomic structure. Magnetic structures often are commensurate with the atomic structure but they can be incommensurate. Three dimensional materials can host a variety of complex magnetism from frustrated magnetism, interesting spin orientations, canting of moments, spiral or helical long range order, glassy or frozen spin states, and potential spin liquid states.

Elastic neutron diffraction can be performed using either a flux or spallation neutron source. High angular resolution in the elastic channel, a well monochromated neutron beam (well defined wavelength of neutron without sacrificing all the intensity of the beam), and reasonable counting statistics are key for the clean diffraction patterns and efficient use of experimental beamtime. For this investigation, the powder diffractometer located at instrument line C2 in Chalk River National Laboratories was used for powder neutron diffraction with instrument scientist Roxana Flacau. The angular spread of the detector allows for 80 degrees to be measured simultaneously. It is also on a moveable track so that two sets of data are able to cover a full spectrum of angles in order to do very accurate refinements. The neutron wavelength can be tuned between 1-4$\mathring{A}$, a resolution of $\sim$0.6 degrees (optional collimators can increase this resolution to $\sim$0.4 or $\sim$0.2 degrees depending on the collimator used)[15].

Inelastic neutron scattering involves interactions between the neutron and the sample where the neutron's incident and final energy are not necessarily the same. For example, this can occur when the neutron loses energy to the sample and creates a phonon excitation in the sample. Q-independent features correspond to localized phenomena in real space such as energy levels on approximately free atom sites. Magnetic excitations are most clearly detectable at low q values and the strength of the scattering goes like the moment on the atom squared.

The inelastic neutron scattering measurements for this investigation were performed on the SEQUIOA beamline at the Spallation Neutron Source (SNS) in Oak Ridge National Laboratories [16]. SEQUIOA is a fine resolution Fermi chopper spectrometer which means it utilizes a series of choppers which allows for the a well defined neutron incident energy[17]. The choppers consist of rotating blades which are made of a neutron absorbing material. Thus by choosing the rotation speed of the choppers, only neutrons with particular incident energies will be able to pass through. SEQUIOA has an incident energy range of ∼4-2000 meV. This energy range is on the order of typical crystal field level excitations, Jahn-Teller distortions, acoustic phonons, low energy optical phonons and can allow for the investigation of low lying excitations such as spin gaps. The detector chamber used by SEQUIOA is wall-papered with neutron detectors in order to give a vertical coverage of ∼-18 to 18 degrees and a horizontal overage of ∼-30 to 60 degrees. This allows for a large coverage in reciprocal space Q while simultaneously exploring a range of neutron energy changes between incident and final energy. Neutrons which have did not gain or lose energy compromise the elastic channel (energy change of zero) and can be used to extract information on elastic diffraction with the sample. By looking at the Q dependence of the features in the inelastic, physical phenomena can be identified and compared to theoretical predictions.

Chapter 3

Results

3.1 Ba_2YAO_6 where A=(Ru,Re,Os)

Ba_2YRuO_6 was synthesized by mixing stoichiometric amounts of $BaCO_3$, Y_2O_3 and RuO_2, packing the well ground mixture into a platinum crucible and reacting for four days in air at 1200^{o}C with one intermittent regrinding. For Ba_2YOsO_6, a stoichiometric combination of $Ba_4Y_2O_7$, and Os with 10% excess Os was mixed and packed into a platinum crucible and reacted in air at 1400^{o}C for one and half hours with one intermittent regrinding. Os metal can react with the air when heated to form gaseous by-products so it is essential to use a furnace such as a box furnace which has been preheated to 1400^{o}C in order to reduce the formation of gaseous by-products. $Ba_4Y_2O_7$ was used after attempts using $BaCO_3$, BaO_2, and Y_2O_3 were unable to produce samples of high enough purity. $Ba_4Y_2O_7$ can be produced by mixing stoichiometric amounts of $BaCO_3$ and Y_2O_3 and reacting at 1000^{o}C in air with one intermittent regrinding. $Ba_4Y_2O_7$ is a metastable phase so a box furnace is used to quench the sample from 1000^{o}C to room temperature relatively quickly. Both Ba_2YRuO_6 and Ba_2YOsO_6 acquired oxygen from the air in order to acquire an oxidation state of +5 for Ru and Os. In the case of Ba_2YReO_6, a 1:5 ratio of Re:ReO_3 was used along with stoichiometric amounts of $BaCO_3$ and Y_2O_3 in order to ensure an average rhenium oxidation state of +5. This mixture was then packed into a platinum crucible, placed in a high temperature tube furnace and argon gas was flowed for six hours to purge the tube. After purging, the argon flow was reduced and the mixture was heated to 1200^oC for two days. Purity of the all the samples were then checked by x-ray diffraction and additional regrindings and refirings were performed accordingly. The electron configurations for Ru^{5+},Re^{5+}, and Os^{5+} are $4d^3$, $5d^2$, and $5d^3$ respectively.

The Ba_2YAO_6 series where A=(Ru,Re,Os) all form in the cubic Fm-3m space group. X-ray powder diffraction data were collected using a PANAlytical X-pert diffractometer using $Cu_{K\alpha1}$ radiation ($\lambda = 1.54056\AA$) at ambient temperature for all samples over the range 10^o to 120^o in 2θ. The data were then imported into the FullProf Suite and the Rietveld[11] software was used to create fits to the powder x-ray data to extract the lattice parameters and the O^{2-} positional parameters for these compounds. Shown in Figure 3.1 is a representative Rietveld fit where the data are shown in red, the black curve is the fit, the blue ticks are expected locations for Bragg peaks, and the blue line is the difference between the data and the fit.

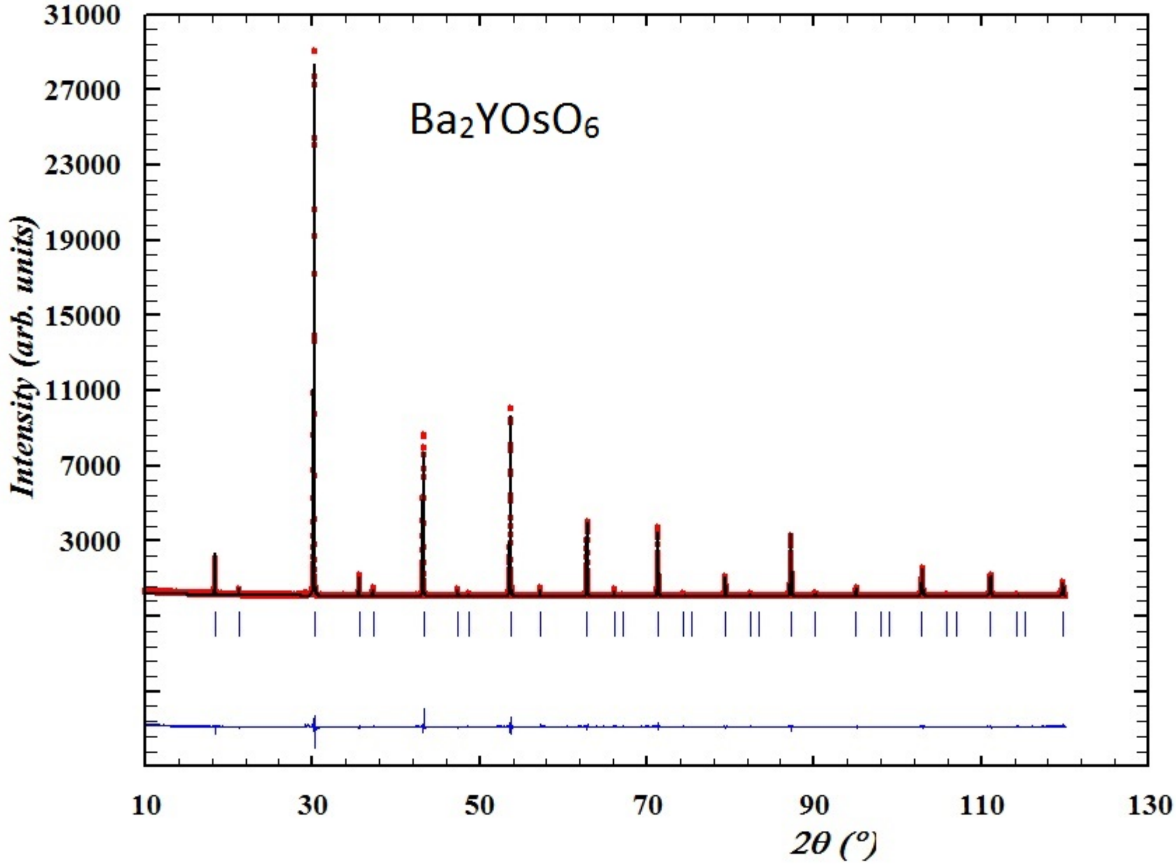

Figure 3.1: Rietveld refinement of Ba_2YOsO_6 at room temperature where the data is shown with red dots, the fit is the black line, the blue ticks indicate predicted structural peaks, and the blue line shows the difference between the data and the fit.

The room temperature lattice parameters for the Ba_2YRuO_6, Ba_2YReO_6 and Ba_2YOsO_6 are $8.3376(4)\AA$, $8.3986(3)\AA$, and $8.3560(1)\AA$ respectively.

For Ba_2YAO_6 (where A=Ru,Re,Os), zero field cooled (ZFC) and field cooled (FC) magnetic susceptibility measurements were performed using a SQUID magnetometer with an applied field of 0.05 T.

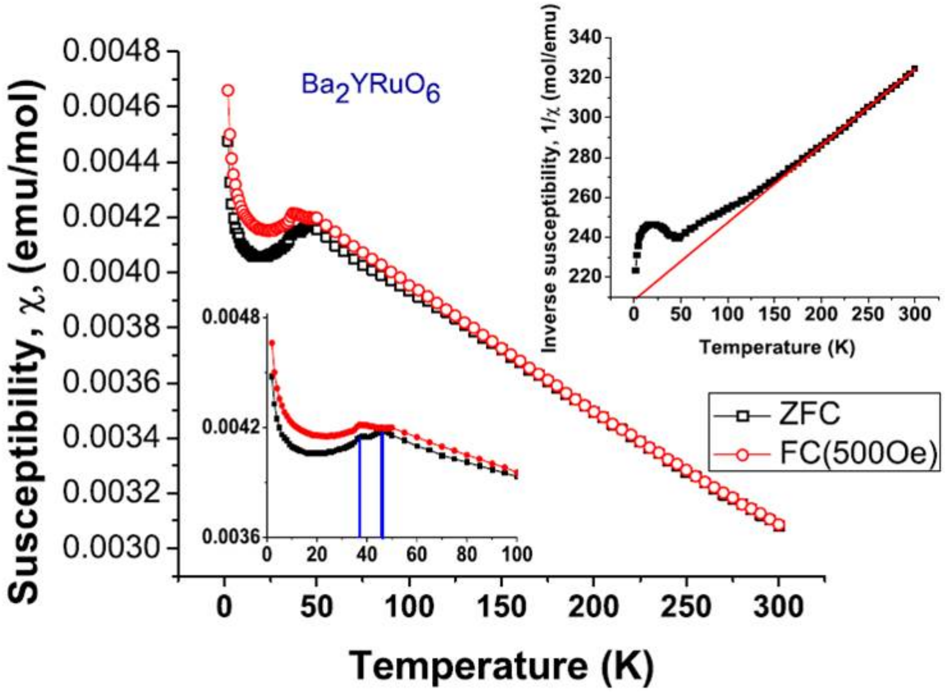

Figure 3.2: ZFC magnetic susceptibility measurements on Ba_2YRuO_6. Inset: Inverse susceptibility of the ZFC data for Ba_2YRuO_6. Plot from [1]

Magnetic susceptibility measurements on Ba_2YRuO_6 shown in Figure 3.2 indicate a magnetic phase transition to an antiferromagnetic ordered state at $\sim$ 36K. Using a Curie-Weiss fit in the high temperature linear region in the inverse susceptibility data gives the following values: C=1.69(1) emu-K/mole, θ_c=-402(3)K, and $\mu_{eff} = 3.67(3)\mu_B$.

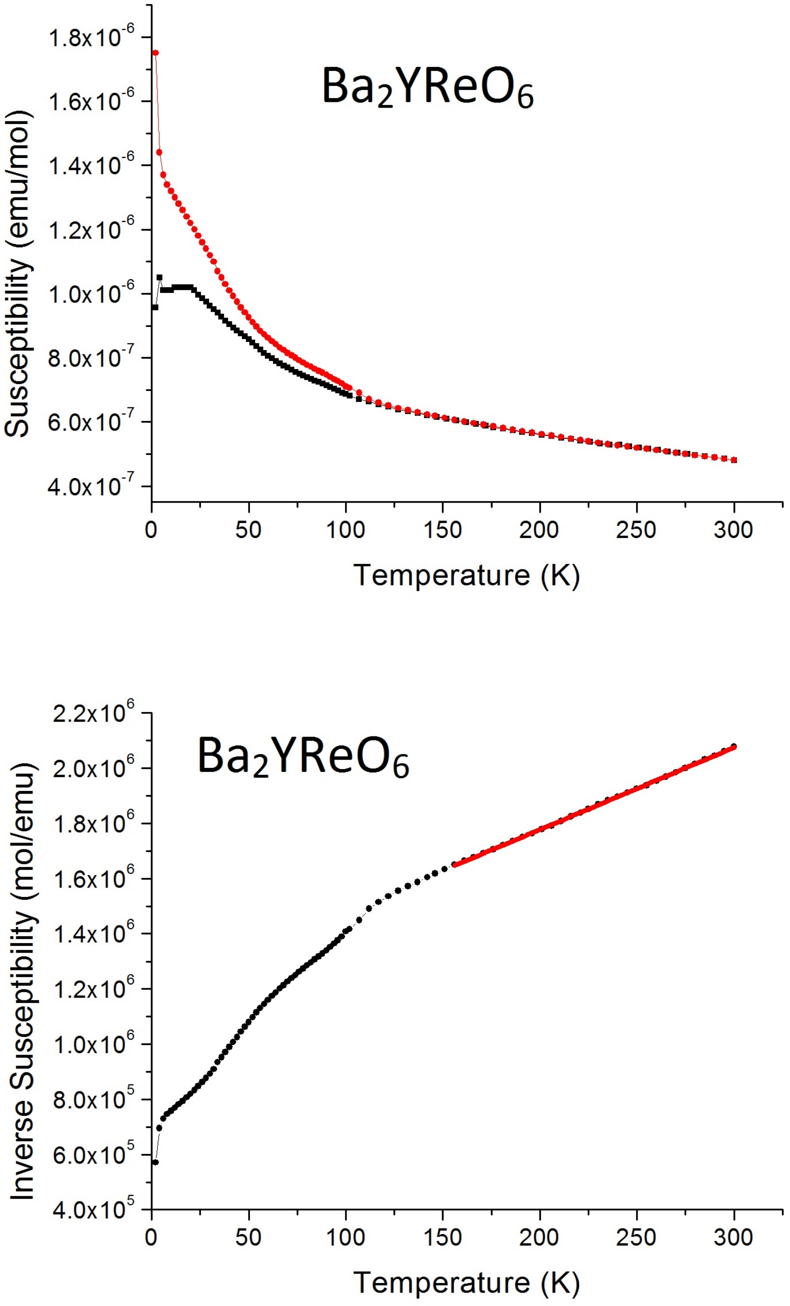

Figure 3.3: On top: ZFC(shown in black) and FC(shown in red) magnetic susceptibility measurements on Ba_2YReO_6. On bottom: Inverse susceptibility of the FC data for Ba_2YReO_6

Magnetic susceptibility measurements (Figure 3.3) on Ba_2YReO_6 show a divergence in the ZFC and FC to a glassy system with antiferromagnetic interactions given by θ_c=-398(3)K.

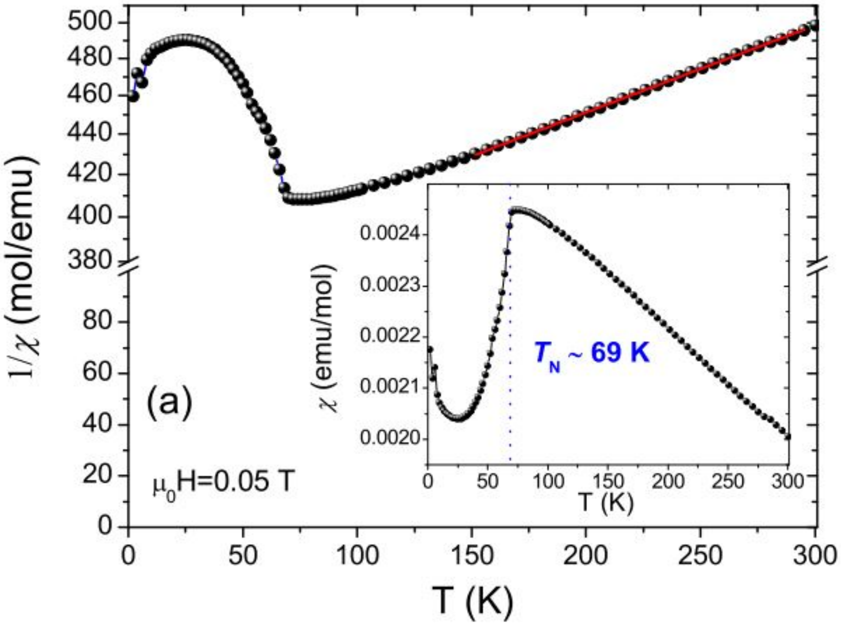

Figure 3.4: ZFC magnetic susceptibility measurements on Ba_2YOsO_6. Inset: Inverse susceptibility of the ZFC data for Ba_2YOsO_6. Plot from [2]

Magnetic susceptibility measurements on Ba_2YOsO_6 show a magnetic phase transition to an antiferromagnetic ordered state at $\sim$ 69K (Figure 3.4). No divergence between the FC and ZFC data is observed. Using a Curie-Weiss fit to data in the high temperature linear region gives the following values: C=2.154(8) emu-K/mole, θ_c=-772(4)K, and $\mu_{eff} = 4.15\mu_B$.

Elastic neutron diffraction experiments on Ba_2YRuO_6 and Ba_2YOsO_6 were performed independently at the powder diffractometer at the C2 instrument at Chalk River National Laboratories[1]. In previous work the Ba_2YRuO_6 was determined to have an ordered moment of $2.1(2)\mu_B$ with an ordering wave vector of k(001)[1]. The ordered moment of $1.65(6)\mu_B$ with ordering wave vector of k(001) for Ba_2YOsO_6 was determined using the k-search function of the Rietveld refinement suit in conjunction with a Rietveld refinement (Figure 3.5 and Figure 3.6). As one would expect from a less than half filled outer shell, the moment on the Os^{5+} ion is smaller than the moment on the Ru^{5+} ion due to hybridization of Os^{5+} with the O^{2-} ligands. The increased covalency of the Os^{5+} ($5d^3$) relative to Ru^{5+} ($4d^3$) would also reduced the ordered moment.

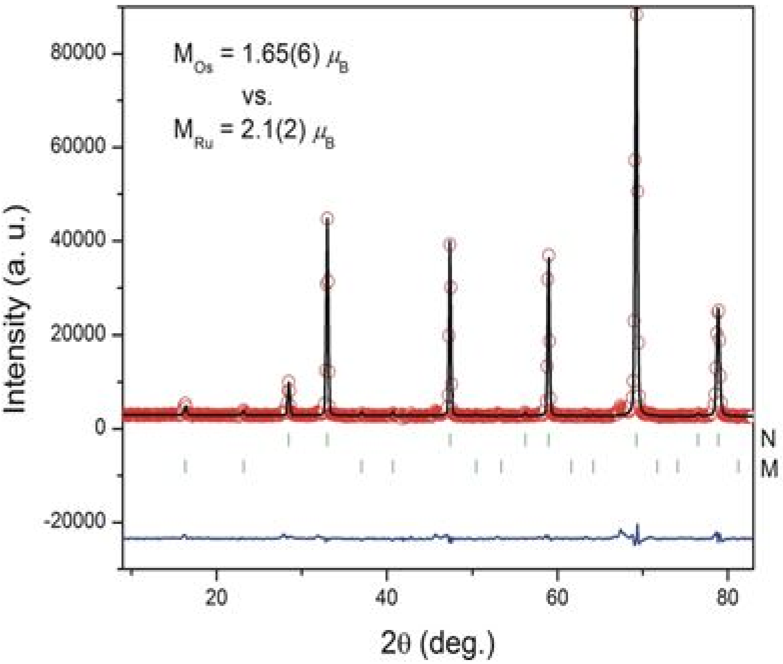

Figure 3.5: Rietveld refinement on elastic neutron diffraction Ba_2YOsO_6 for both the nuclear and magnetic structure where the series of N markings denote the location of nuclear peaks and the M markings denote the location of magnetic peaks.

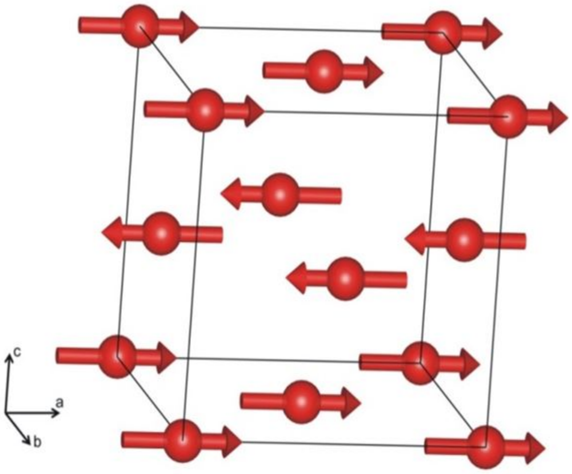

Figure 3.6: Magnetic structure of $Ba_2Y(Ru,Os)O_6$ from Rietveld refinement with ordering wave vector k(001).

Inelastic neutron scattering experiments on Ba_2YRuO_6 and Ba_2YOsO_6 were performed independently at the SEQUIOA beamline at the SNS at Oak Ridge National Laboratories. Ba_2YRuO_6 was investigated in previous work to have a spin gap in the low q region with a gap energy of ∼5meV[3]. Investigation of Ba_2YOsO_6 by Edwin Kermarrec displayed a spin gap in the low q region but with a much larger spin gap energy of ∼17meV.

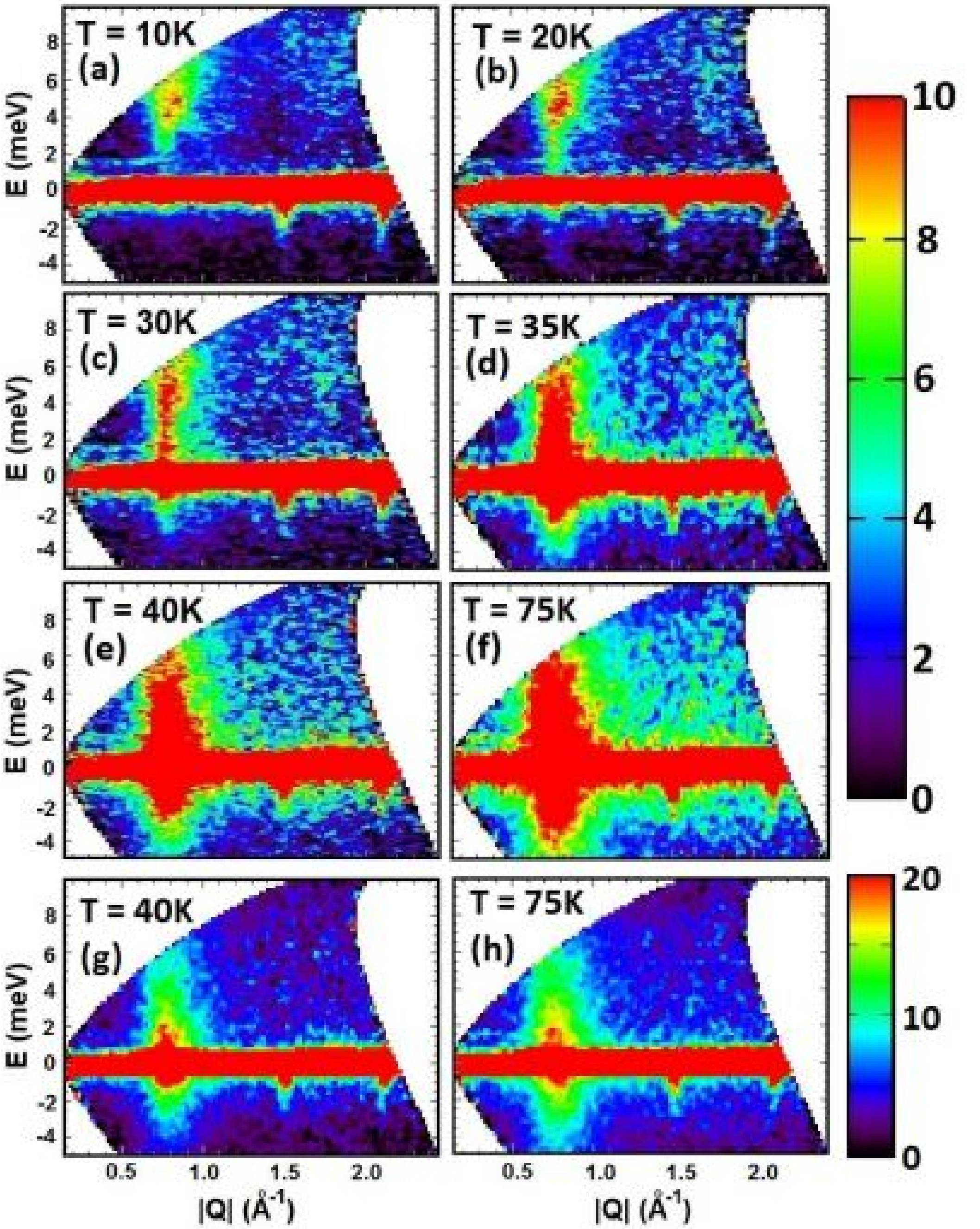

Figure 3.7: Plot of inelastic neutron scattering of Ba_2YRuO_6 showing the formation of the spin gap of 5meV taken from [3].

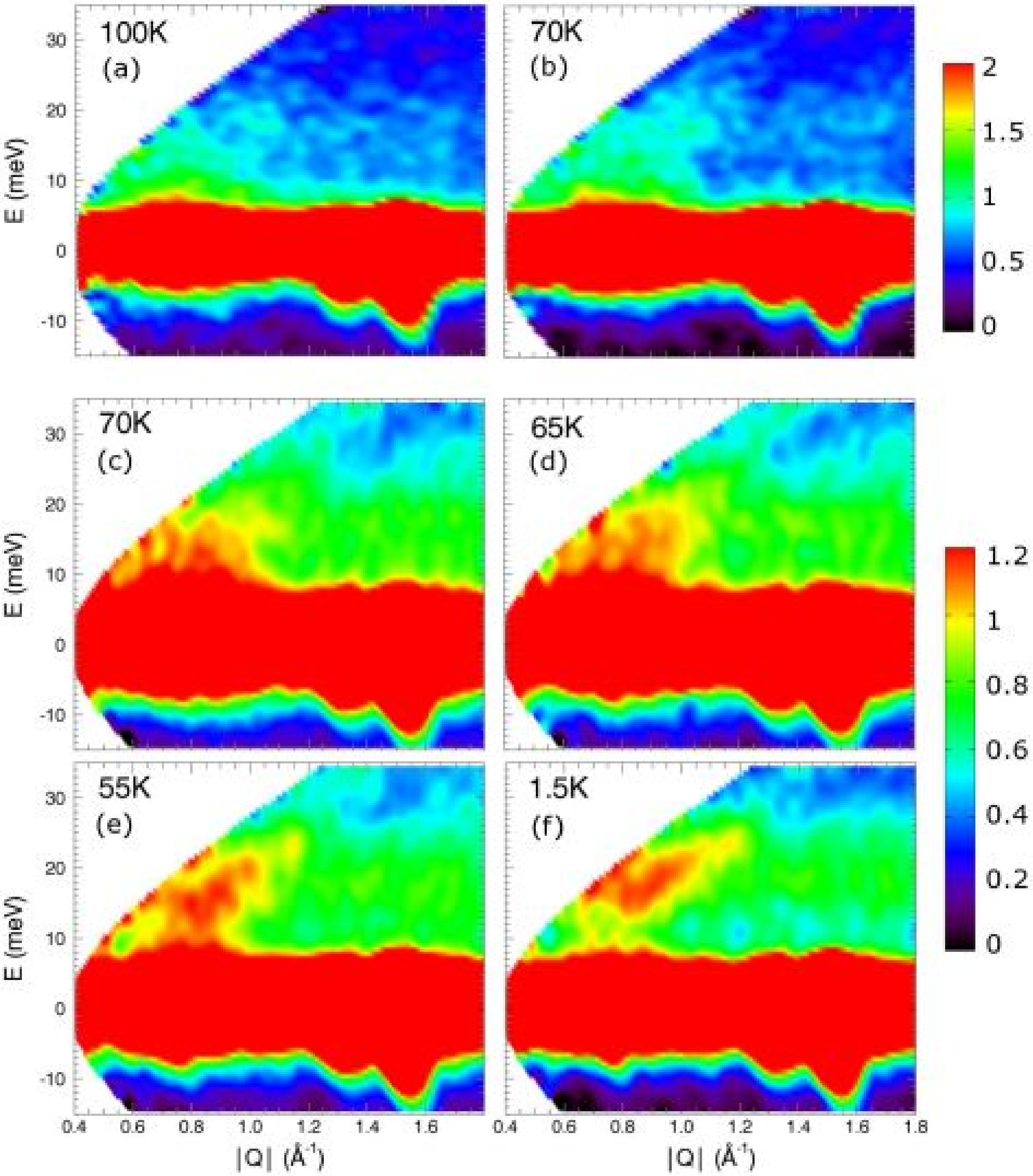

Figure 3.8: Plot of inelastic neutron scattering of Ba_2YOsO_6 showing the formation of the spin gap of 17meV from[2].

3.2 Ba_2MReO_6 where M=(Mg,Zn,$Y_{2/3}$)

The $BaMReO_6$ where (M=Mg,Zn,$Y_{2/3}$) compounds were prepared by conventional solid state reactions. For all the compounds in this system, the rhenium oxidation state is 6+ which gives an electron configuration of $5d^1$. Stoichiometric amounts of $BaCO_3$, MgO, ZnO, Y_2O_3 and ReO_3 were ground together and heated in argon for two days in a platinum crucible at 1200^oC for M=Mg,$Y_{2/3}$ and 1000^oC for M=Zn. The prepared samples were characterized as single phase using x-ray diffraction. In addition, the isostructural series Ba_2MWO_6 were prepared to serve as non-magnetic analogues to the rhenium compounds for an approximation of the lattice contribution to the specific heat. Stoichiometric amounts of $BaCO_3$, MgO, ZnO, and WO_3 were ground together and heated in air for two days in an alumina crucible at 1200^oC for M=Mg,Zn. In order to produce a phase pure $Ba_2Y_{2/3}WO_6$, first $BaCO_3$, 10% deficient Y_2O_3, and WO_3 were ground together and heated to 1400^oC for two days in a tube furnace with an atmosphere of argon 5% hydrogen. The resulting dark blue powder was then heated for three hours in air at 700^oC.

The Ba_2MReO_6 and Ba_2MWO_6 series where M=(Mg,Zn,$Y_{2/3}$) all form in the cubic Fm-3m space group. X-ray powder diffraction data were collected using a PANAlytical X-pert diffractometer using $Cu_{K\alpha 1}$ radiation ($\lambda = 1.54056\mathring{A}$) at ambient temperature for all samples over the range 10^o to 120^o in 2θ. This data was then imported into the FullProf Suite and the Rietveld[11] software was used to create fits to the powder x-ray data to extract the lattice parameters for these compounds. Shown in Figure 3.9 is a representative Rietveld fit where the data is shown in red, the black curve is the fit, the blue ticks are expected locations for Bragg peaks, and the blue is the difference between the data and the fit.

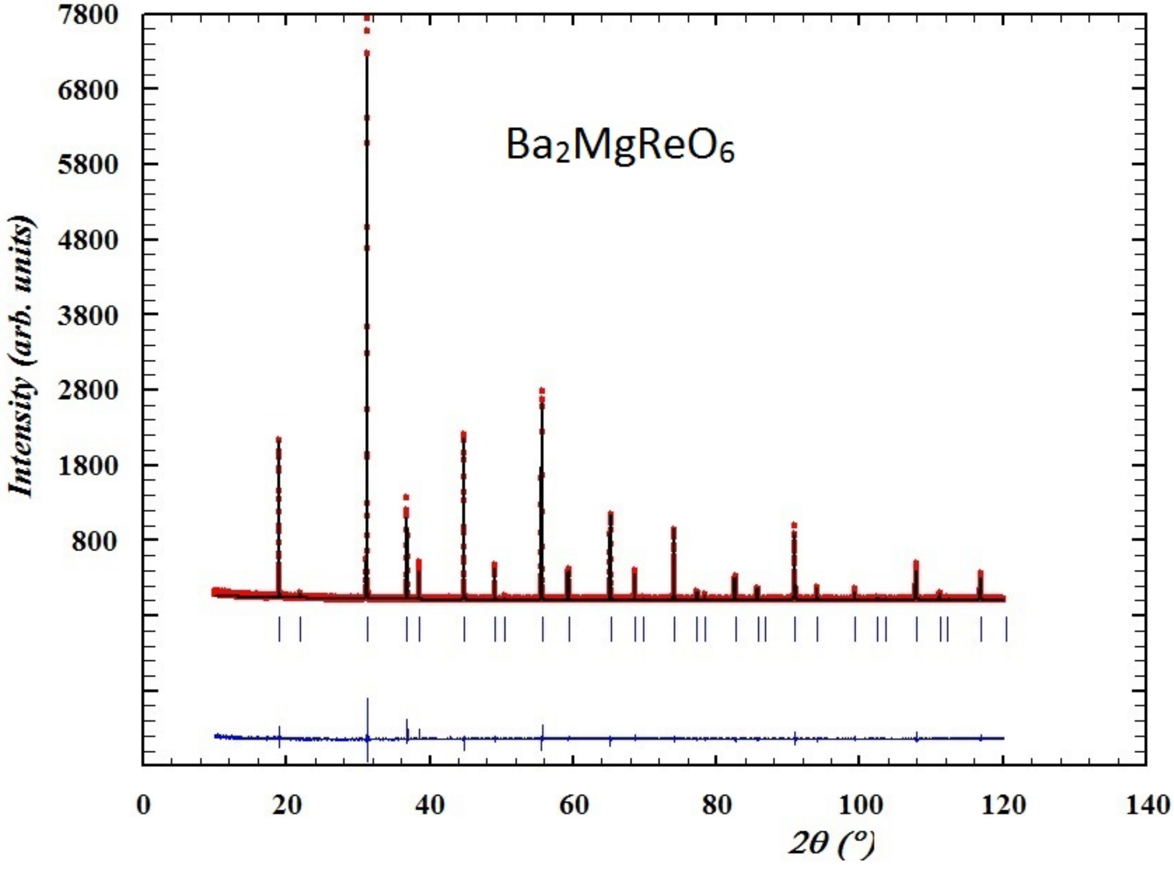

Figure 3.9: Rietveld refinement of Ba_2MgReO_6 at room temperature where the data is shown with red dots, the fit is the black line, the blue ticks indicate predicted structural peaks, and the blue line shows the difference between the data and the fit.

The room temperature lattice parameters for the Ba_2MgReO_6, Ba_2ZnReO_6, $Ba_2Y_{2/3}ReO_6$, Ba_2MgWO_6, Ba_2ZnWO_6, and $Ba_2Y_{2/3}WO_6$ are $8.0849(2)\mathring{A}$, $8.1148(1)\mathring{A}$, $8.3602(2)\mathring{A}$, $8.10313(6)\mathring{A}$, $8.12056(9)\mathring{A}$, and $8.38412(9)\mathring{A}$ respectively.

For Ba_2MReO_6 (where M=Mg,Zn,$Y_{2/3}$), zero field cooled (ZFC) and field cooled (FC) magnetic susceptibility measurements were performed using a SQUID magnetometer with an applied field of 0.05 T. Magnetization measurements were taken at 2K over an applied field range of -5 to 5T.

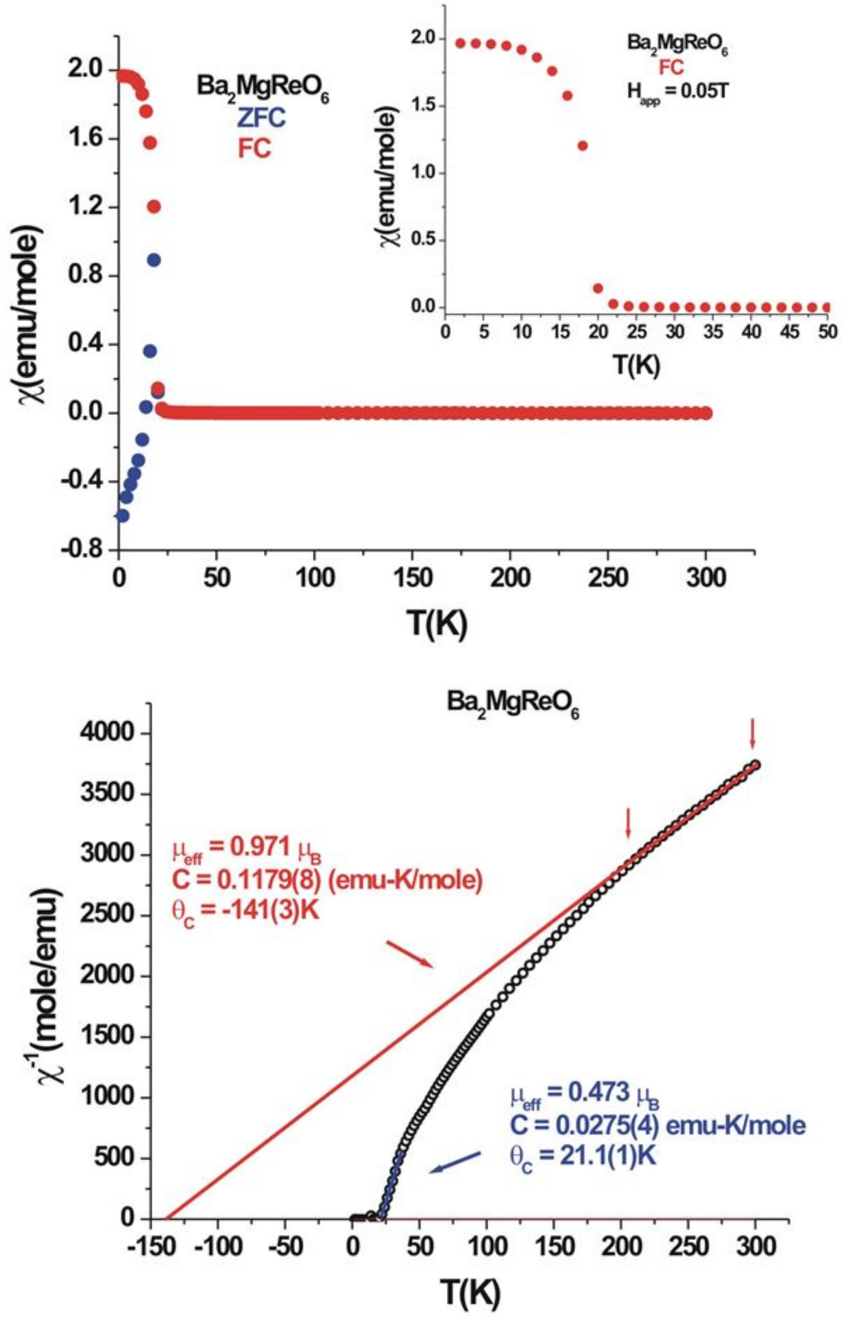

Figure 3.10: On top: ZFC(shown in blue) and FC(shown in red) magnetic susceptibility measurements on Ba_2MgReO_6. On bottom: Inverse susceptibility of the FC data for Ba_2MgReO_6

Magnetic susceptibility measurements on Ba_2MgReO_6 shows a transition temperature around ∼16 K with to a ferromagnetic ordered state (Figure 3.10). Depending on the linear region chosen in the inverse magnetic susceptibily data for Ba_2MgReO_6, two sets of Curie constants, Weiss constants θ_c, and effective moments can be extracted using the Curie-Weiss model. High temperature fits give the values C=0.1179(8)emu-K/mole, θ_c=-141(3)K, and $\mu_{eff} = 0.971\mu_B$. The large negative value would lead one to conclude antiferromagnetic interactions are occurring which does not appear to be consistent with the behaviour of the system at the ordering temperature. A fit taken in a linear region of the inverse susceptibility closer to the transition temperature give the values C=0.0275(4)emu-K/mole, θ_c=21.1(1)K, and $\mu_{eff} = 0.473\mu_B$. The fit near the transition temperatures indicates ferromagnetic interactions.

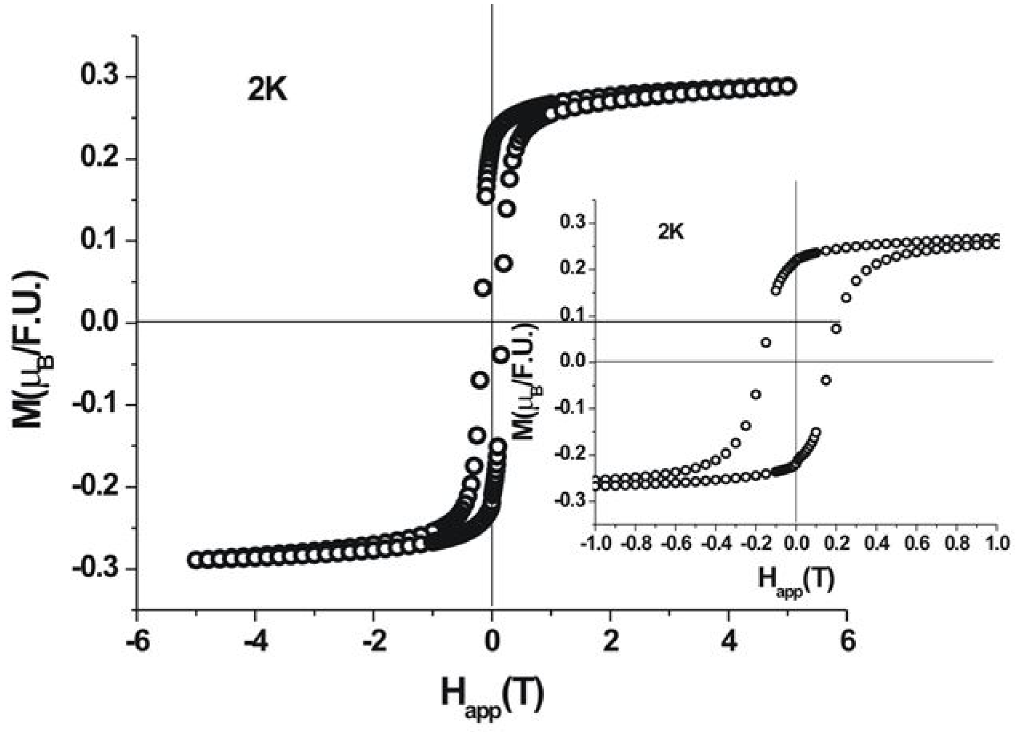

Figure 3.11: Magnetic hysteresis measurements of Ba_2MgReO_6 at 2K

The magnetic hysteresis measurements, shown in Figure 3.11, on Ba_2MgReO_6 indicate a coercivity of ∼0.2 T with a saturated magnetic moment of $\sim 0.3\mu_B$. The presence of coercivity in magnetic hysteresis suggests that this system is ferromagnetic below the transition temperature. Additionally, the value of the the saturated magnetic moment is sufficiently large to exclude the possibility of a canted antiferromagnetic system.

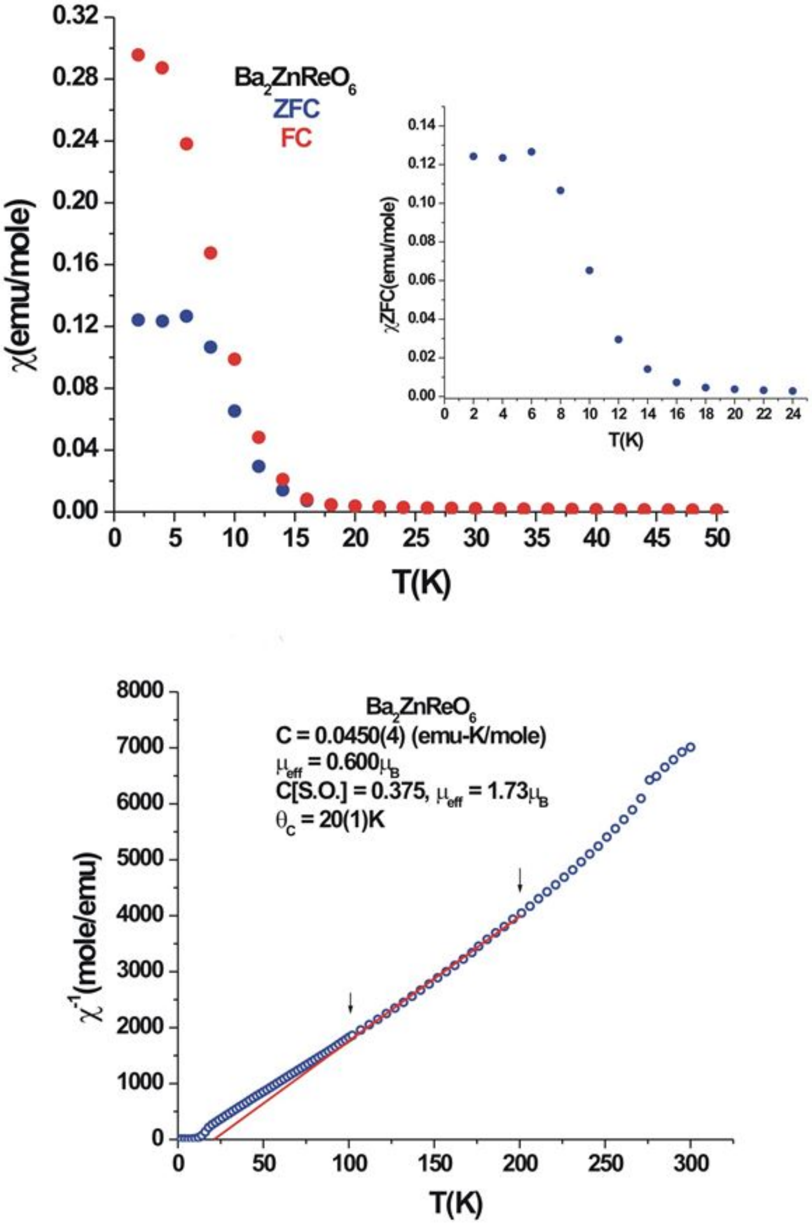

Figure 3.12: On top: ZFC(shown in blue) and FC(shown in red) magnetic susceptibility measurements on Ba_2ZnReO_6. On bottom: Inverse susceptibility of the ZFC data for Ba_2ZnReO_6

Magnetic susceptibility measurements on Ba_2ZnReO_6 show a magnetic phase transition to a ferromagnetic ordered state at $\sim$ 16K (Figure 3.12). Using a Curie-Weiss fit in the high temperature linear region in the inverse susceptibility data gives the following values: C=0.0450(4)emu-K/mole, θ_c=20(1)K, and $\mu_{eff} = 0.6\mu_B$.

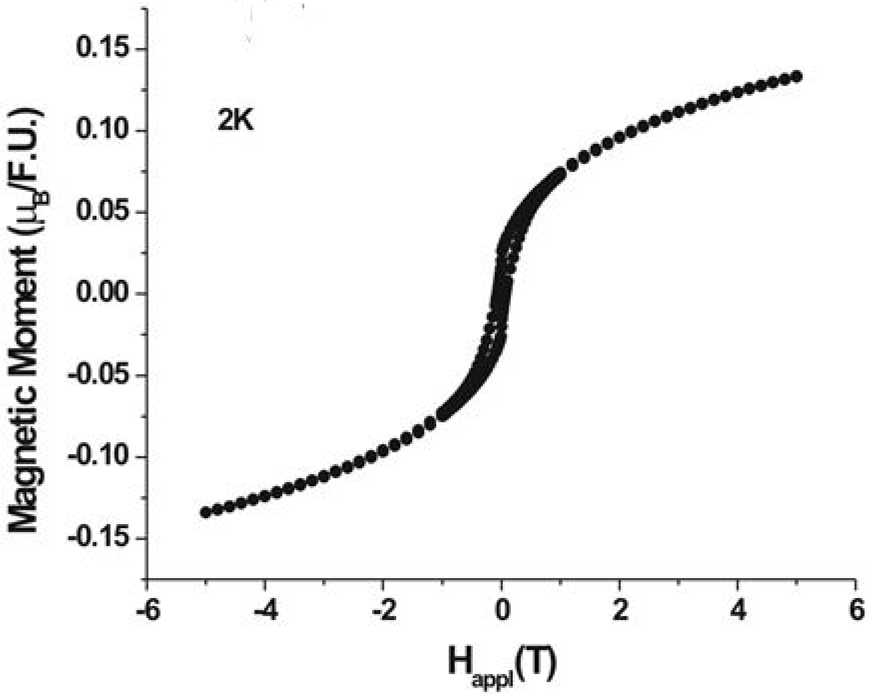

Figure 3.13: Magnetic hysteresis measurements of Ba_2ZnReO_6 at 2K

The magnetic hysteresis measurements, shown in Figure 3.13, on Ba_2ZnReO_6 indicate a coercivity of ~0.08 T with a saturated magnetic moment of $\sim 0.19\mu_B$. The presence of coercivity in magnetic hysteresis suggests that this system is ferromagnetic below the transition temperature.

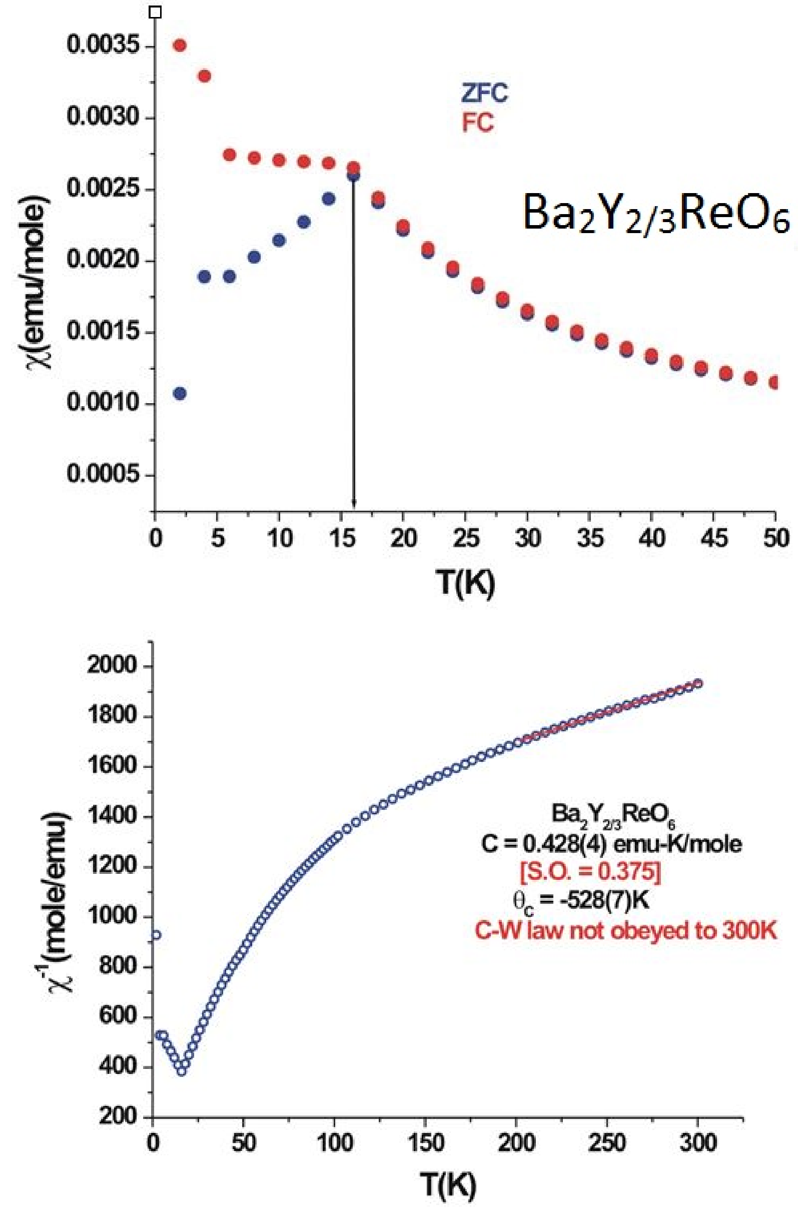

Figure 3.14: On top: ZFC(shown in blue) and FC(shown in red) magnetic susceptibility measurements on $Ba_2Y_{2/3}ReO_6$. On bottom: Inverse susceptibility of the ZFC data for $Ba_2Y_{2/3}ReO_6$

Unlike Ba_2MgReO_6 and Ba_2ZnReO_6 which indicate a ferromagnetic ordered state, $Ba_2Y_{2/3}ReO_6$ demonstrates a spin glass phase transition at ~16K (Figure 3.14). This is characterized by the splitting the ZFC and FC measurements where the FC become almost flat after the transition and ZFC decreases. The behaviour at low temperatures is attributed to impurity. Using a Curie-Weiss fit in the high temperature linear region in the inverse susceptibility data gives the following values: C=0.428(4)emu-K/mole, θ_c=-528(7)K, and $\mu_{eff} = 1.9\mu_B$. Since μ_{eff} is so large compared to the theoretical value, it is likely that a true Curie-Weiss regime is not present.

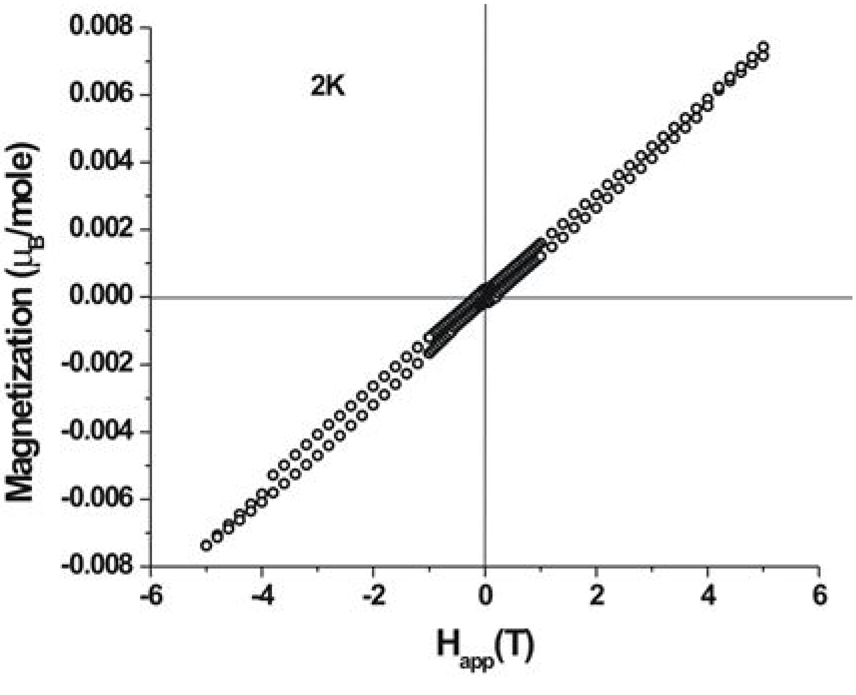

Figure 3.15: Magnetic hysteresis measurements of $Ba_2Y_{2/3}ReO_6$ at 2K

The magnetic hysteresis for $Ba_2Y_{2/3}ReO_6$ shows no saturation (Figure3.15).

Heat capacity measurements were taken over the range of approximately 4K to 45K and compared to the isostructural non-magnetic tungsten compounds. The heat capacity of the isostructural compounds are fit using three parameters (K_1,K_2,K_3)in the form: C_p=K_1T+K_2T^3+K_3T^5. These fits can then be used to subtract an approximation of the non-magnetic contributions to the heat capacity so that only the magnetic portion remains as can be seen in Figure 3.16, Figure 3.17, and Figure 3.18. These approach is not perfect but it can lead to the observation of more subtle features such as Schottky anomalies which would have otherwise been missed.

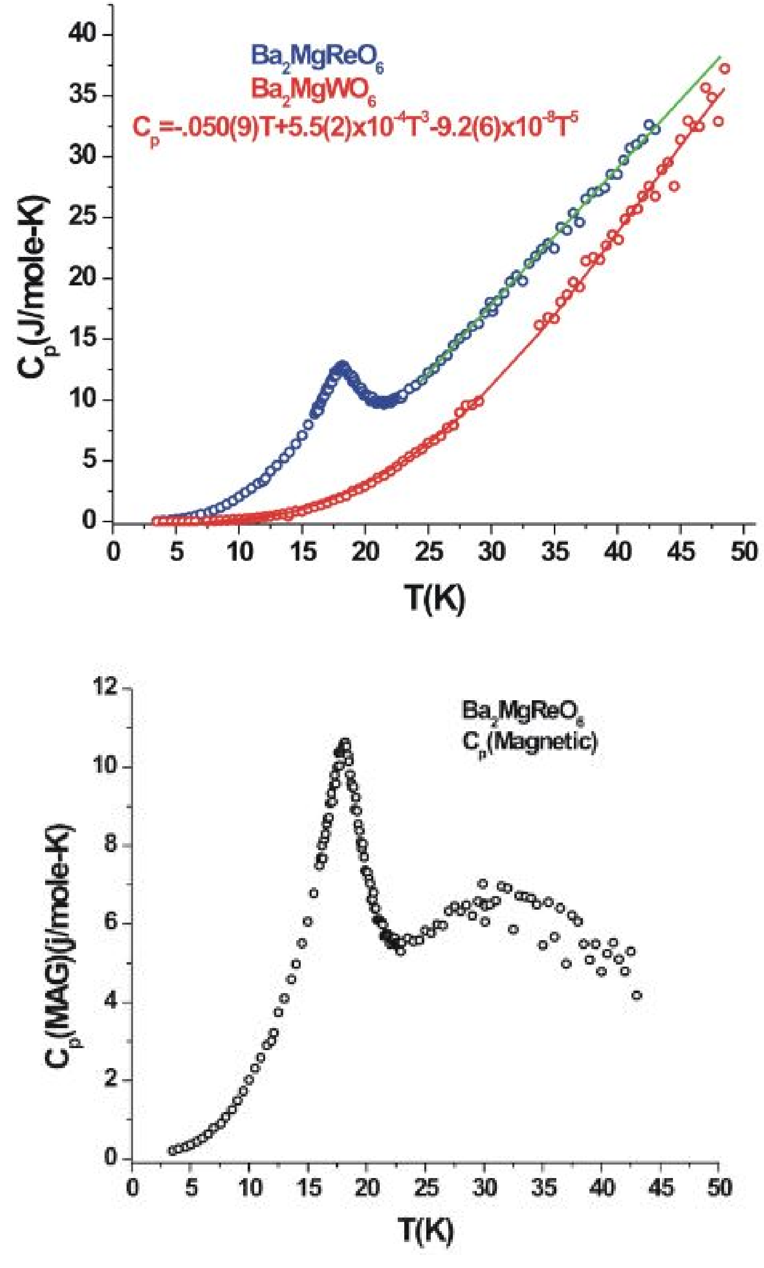

Figure 3.16: On top: Heat capacity of Ba_2MgReO_6 (shown in blue) and Ba_2MgWO_6 (shown in red) with a fit for the Ba_2MgWO_6 data. On bottom: Subtraction of the Ba_2MgWO_6 fit to show the magnetic heat capacity of Ba_2MgReO_6

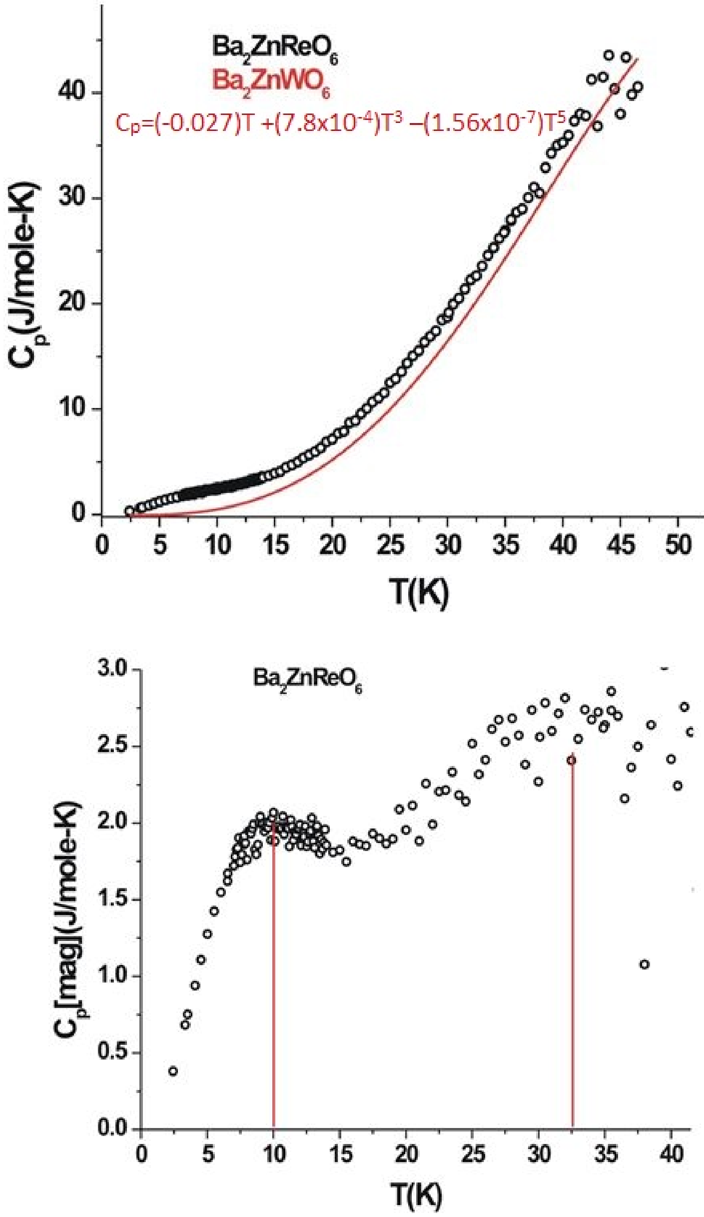

Figure 3.17: On top: Heat capacity of Ba_2ZnReO_6 (shown in black) and Ba_2ZnWO_6 (shown in red) with a fit for the Ba_2ZnWO_6 data. On bottom: Subtraction of the Ba_2ZnWO_6 fit to show the magnetic heat capacity of Ba_2ZnReO_6

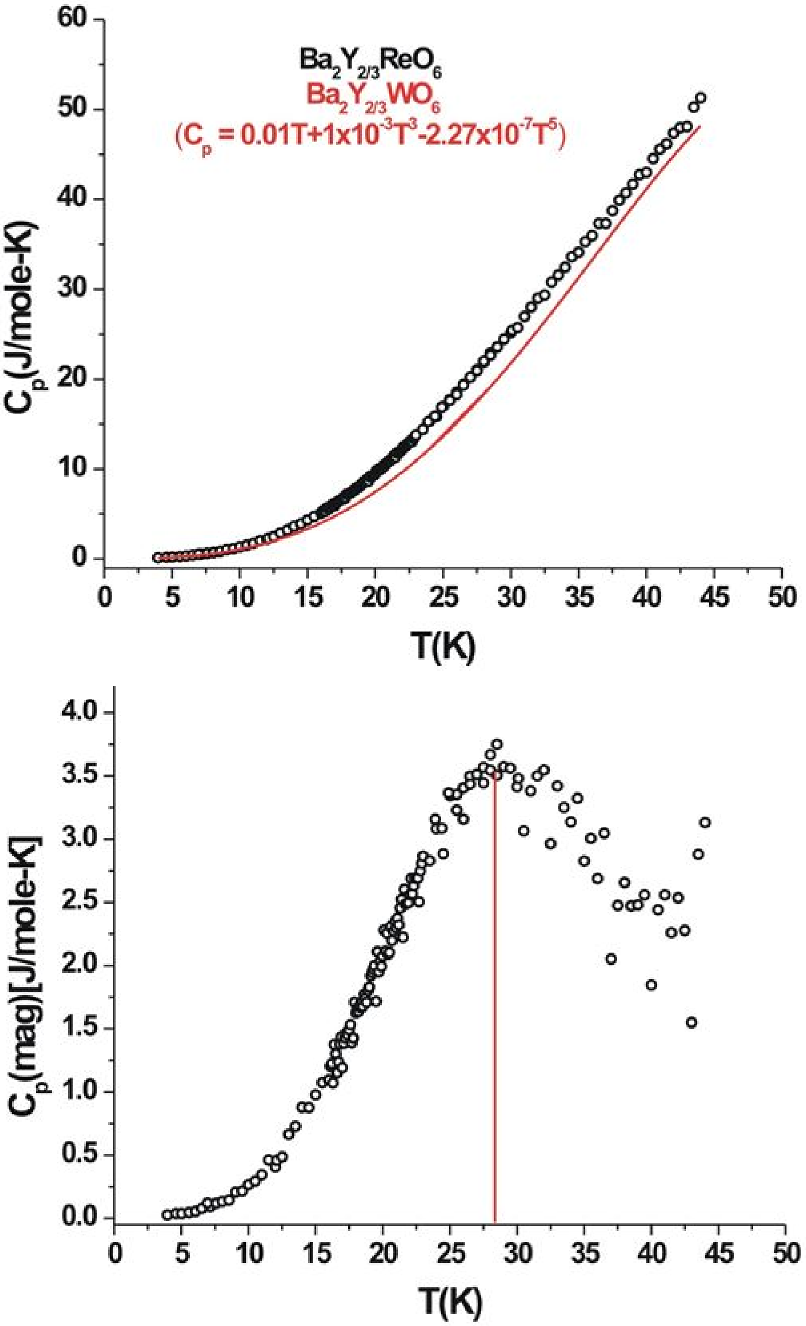

Figure 3.18: On top: Heat capacity of $Ba_2Y_{2/3}ReO_6$ (shown in black) and $Ba_2Y_{2/3}WO_6$ (shown in red) with a fit for the $Ba_2Y_{2/3}WO_6$ data. On bottom: Subtraction of the $Ba_2Y_{2/3}WO_6$ fit to show the magnetic heat capacity of $Ba_2Y_{2/3}ReO_6$

Neutron diffraction experiments were performed on the Ba_2MReO_6 (where M=Mg,Zn,$Y_{2/3}$) series on the powder diffractometer on instrument line C2 at Chalk River National Laboratories. The samples were approximately 2 grams, loaded into vanadium cans, and temperature was controlled using a top-loading closed cycle refrigerator. Two incident wavelengths of neutrons were used, $1.33\AA$ and $2.37\AA$, with measurements taken at 3K and 290K for each wavelength. Due to small moments arising from the $5d^1$ spins, and ferromagnetic ordering (in the case of M=Mg,Zn) or spin glass behaviour ($Y_{2/3}$), no magnetic diffraction peaks could be confirmed. However, it was shown that the unit cell stayed cubic down to the lowest temperatures measured with no detectable splitting of the peaks which would be expected for a Jahn-Teller distortion. Representative diffraction patterns are shown in Figure 3.19.

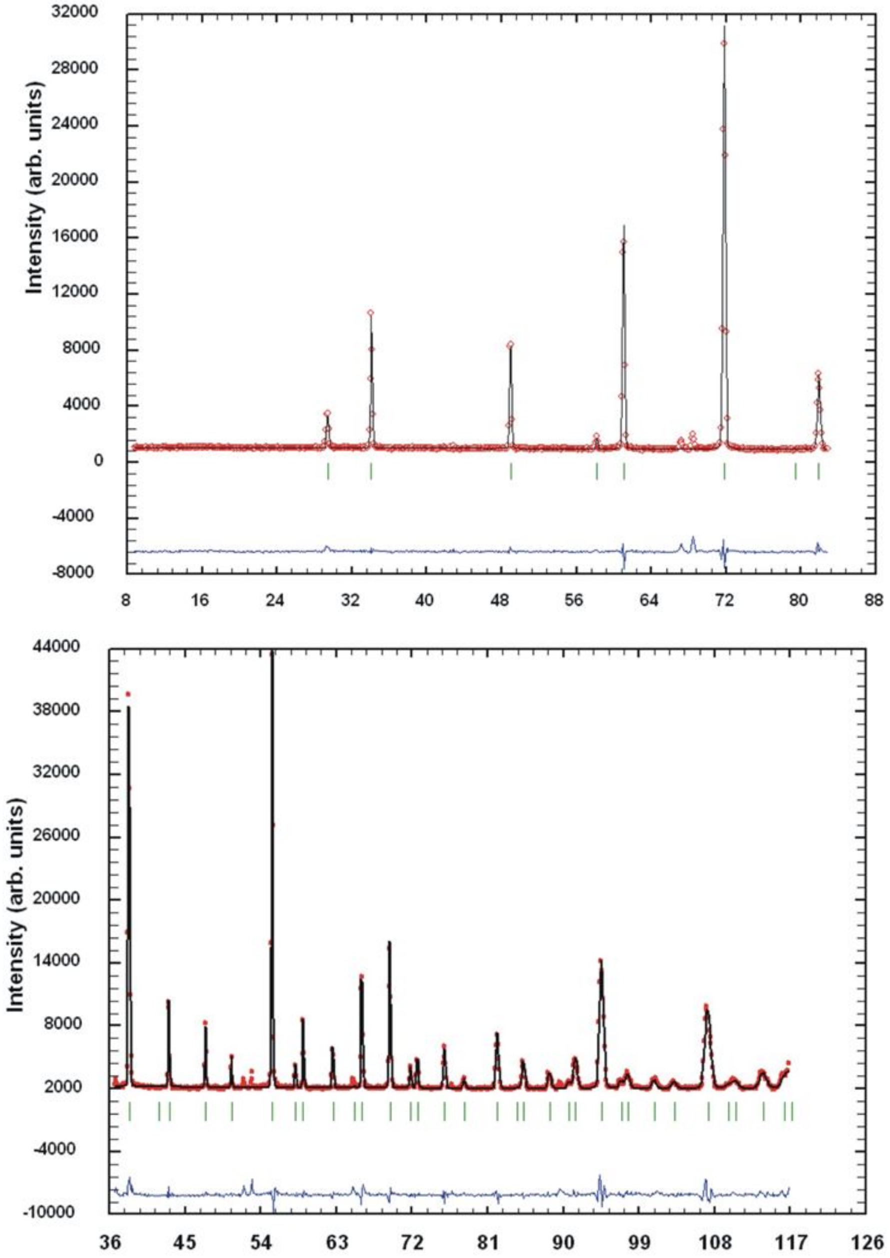

Figure 3.19: Rietveld refinements of neutron powder data at 290K on Ba_2MgReO_6. On top: λ=2.37$\mathring{A}$. On bottom: λ=1.33$\mathring{A}$

Neutron scattering measurements were performed on the Ba_2MReO_6 (where M=Mg,Zn,$Y_{2/3}$) series at the Spallation Neutron Source (SNS, Oak Ridge National Laboratory), on the SEQUOIA Fine Resolution Fermi Chopper Spectrometer [16]. An incident neutron energy of 25meV, 60meV, and 120meV was used with a temperature range of 6K to 70K. The samples were enclosed in annular aluminum cells with a He exchange gas atmosphere and loaded into an Orange 4He-flow cryostat. An identical empty can was measured under the same experimental conditions and used for background subtraction.

Unfortunately due to the low scattering from the $5d^1$ moments, energy resolution, and experimental considerations, the existence or non-existence of a spin gap in these samples could not be confirmed. It is also possible to investigate the potential Jahn-Teller splitting which was not detectable by the elastic neutron diffraction. Assuming that the distortion splits the j=3/2 state into two doublets, δ can be estimated from the standard theory for Schottky anomalies, i.e., δ= T(Cp_{max})/0.417=80K or ~7 meV (Figure 3.20) [18]. This energy lies within the range which is detectable by inelastic neutron scattering. The inelastic neutron scattering data for all three rhenate compounds (Figure 3.21) show no detectable signs of a spin gap or a Jahn-Teller distortion around 7 meV. The features located at 14K are an artifact from a combination of improper shielding and a resulting secondary diffraction of the elastic scattering which arrives at the detectors at a later time than the proper elastic channel. The wave-like features which grow in intensity from low q to high q are attributed to phonons.

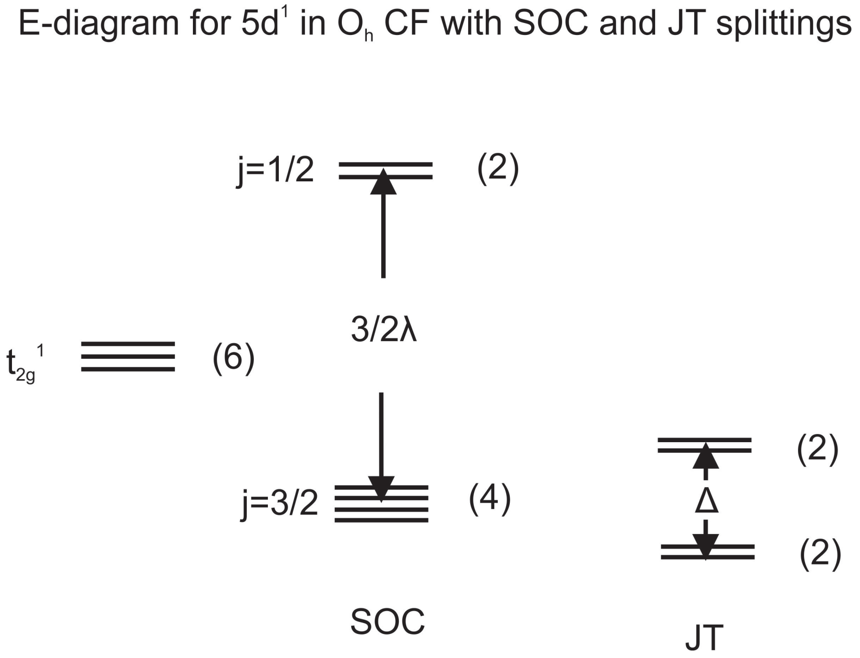

Figure 3.20: Possible energy level scheme for a t2g1 ion subject to SOC and a JT splitting where the numbers in parentheses indicate the state degeneracy.

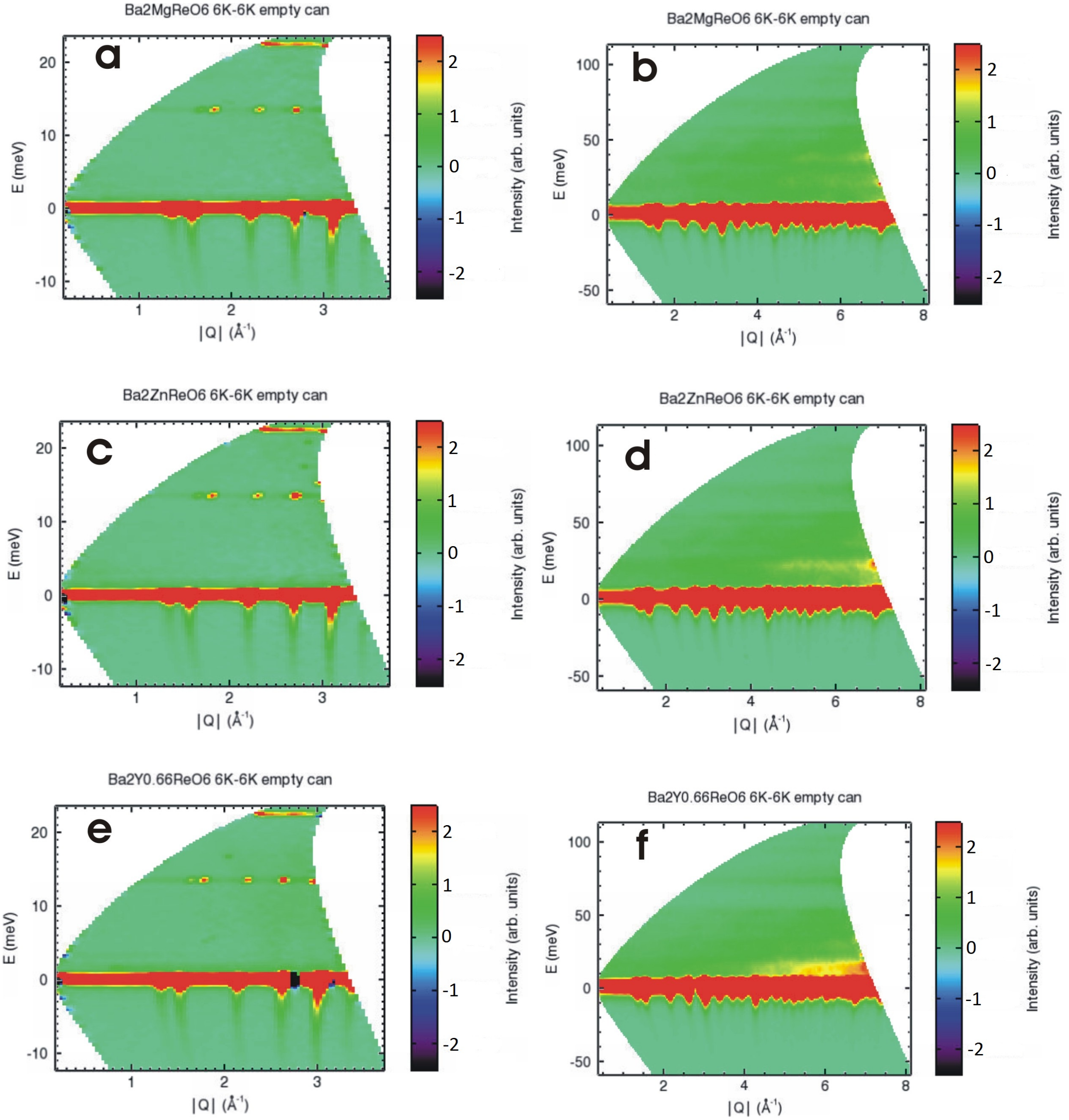

Figure 3.21: Inelastic neutron scattering data for the Ba_2MReO_6 (where M=Mg,Zn,$Y_{2/3}$) series shown with varying incident energy levels including 25meV, 60meV, and 120 meV with empty can subtractions.

3.3 Ba_2GOsO_6 where G=(Mg,Zn,Cd)

The Ba_2GOsO_6 where (G=Mg,Zn,Cd) compounds were prepared by conventional solid state reactions. For all the compounds in this system, the osmium oxidation state is 6+ which gives an electron configuration of $5d^2$. Stoichiometric amounts of BaO_2, MgO, 10% excess ZnO, CdO and 10% excess Os were ground together, packed into a platinum crucible and heated in air at 1000^oC for the following lengths of time: four days for Ba_2MgOsO_6, four hours for Ba_2ZnOsO_6, and one hour for Ba_2CdOsO_6. Similar to the preparation of Ba_2YOsO_6, a box furnace which is preheated to the reaction temperatures in order to avoid slowly heating the Os metal in air and forming gaseous byproducts. In addition, the isostructural series Ba_2GWO_6 were prepared to serve as non-magnetic analogues to the osmium compounds for an approximation of the lattice contribution to the specific heat. Stoichiometric amounts of $BaCO_3$, MgO, ZnO,CdO, and WO_3 were ground together and heated in air for two days in an alumina crucible at 1200^oC for G=Mg,Zn and 1200^oC for Cd.

The Ba_2GOsO_6 series where G=(Mg,Zn,Cd) all form in the cubic Fm-3m space group. X-ray powder diffraction data were collected using a PANAlytical X-pert diffractometer using $Cu_{K\alpha 1}$ radiation ($\lambda = 1.54056 \mathring{A}$) at ambient temperature for all samples over the range 10^o to 120^o in 2θ. This data was then imported into the FullProf Suite and the Rietveld[11] software was used to create fits to the powder x-ray data to extract the lattice parameters for these compounds. Shown in Figure 3.22 is a representative Rietveld fit where the data is shown in red, the black curve is the fit, the blue ticks are expected locations for Bragg peaks, and the blue is the difference between the data and the fit.

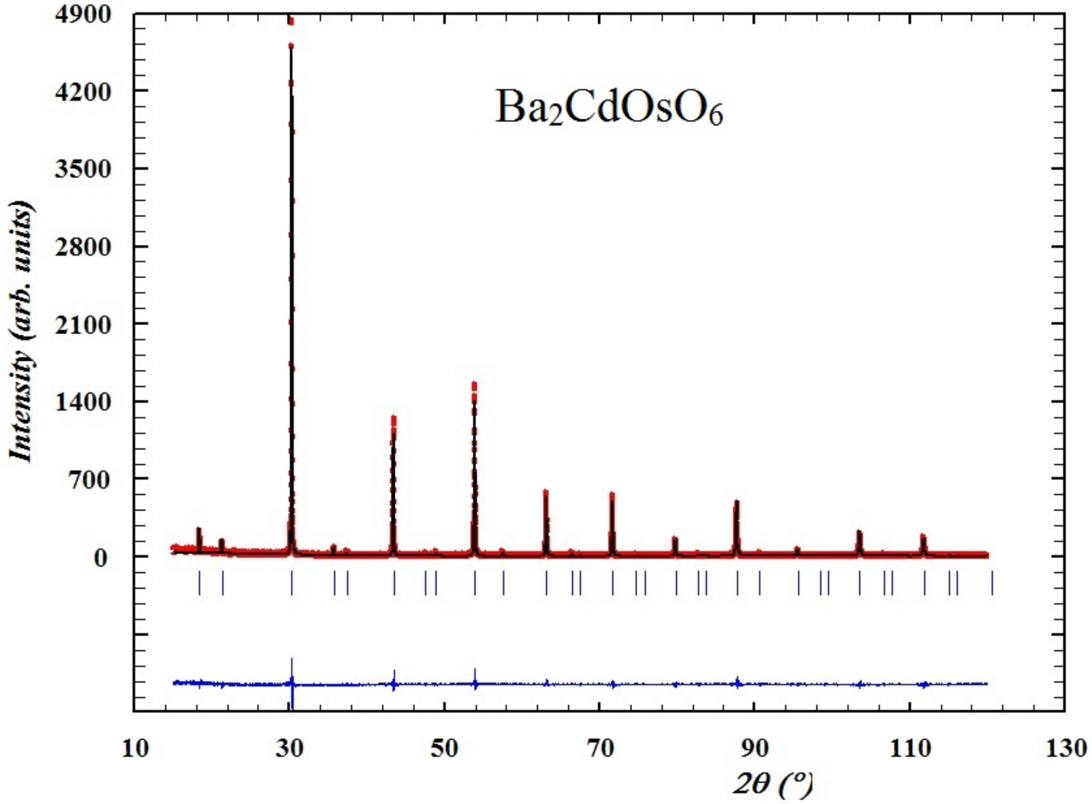

Figure 3.22: Rietveld refinement of Ba_2CdOsO_6 at room temperature where the data is shown with red dots, the fit is the black line, the blue ticks indicate predicted structural peaks, and the blue line shows the difference between the data and the fit.

The room temperature lattice parameters for the Ba_2MgOsO_6, Ba_2ZnOsO_6 and Ba_2CdOsO_6 are $8.0757(1)\AA$, $8.0975(1)\AA$, and $8.3190(1)\AA$ respectively.

For Ba_2GOsO_6 (where G=Mg,Zn,Cd), zero field cooled (ZFC) and field cooled (FC) magnetic susceptibility measurements were performed using a SQUID magnetometer with an applied field of 0.1 T. Magnetization measurements were taken at 2K over an applied field range of -5 to 5T. All of the Ba_2GOsO_6 were found to contain some amount (on the order of a few percent) of impurity phase $Ba_4Os_{11}O_{24}$ which is known to have a weak ferromagnetic transition at 6K [19]. This impurity was not always possible to detect in the x-ray diffraction data but was present all the magnetic susceptibility and magnetic hysteresis measurements. Therefore all ferromagnetic behaviour occurring at 6K and below is attributed to the impurity phase as well as small coercivity in the hysteresis measurements which were taken at 2K.

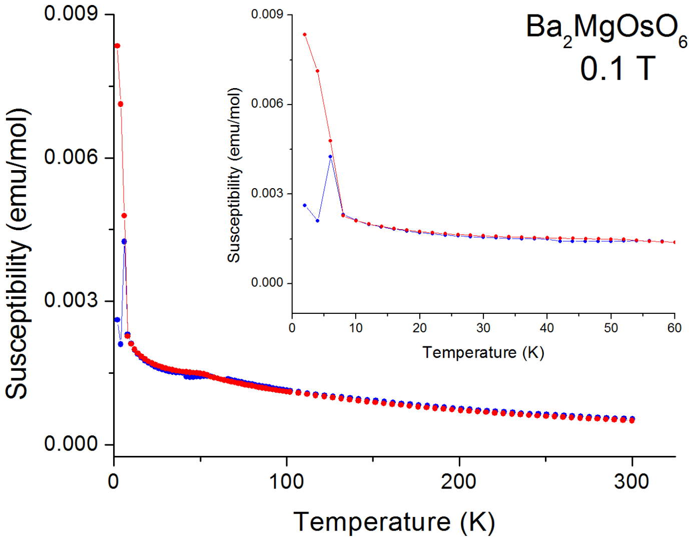

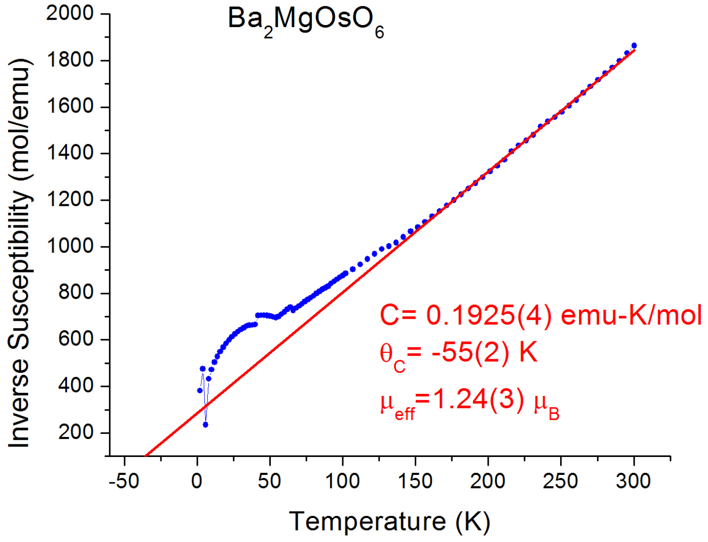

Figure 3.23: On top: ZFC(shown in blue) and FC(shown in red) magnetic susceptibility measurements on Ba_2MgOsO_6. On bottom: Inverse susceptibility of the FC data for Ba_2MgOsO_6

Magnetic susceptibility measurements on Ba_2MgOsO_6 show a ZFC/FC divergence around 10 K and a possible transition temperature at ~45K with antiferromagnetic interactions (Figure 3.23). Using a Curie-Weiss fit in the high temperature linear region in the inverse susceptibility data gives the following values: C=0.192(5)emu-K/mole, θ_c=-51(2)K, and $\mu_{eff} = 1.2\mu_B$.

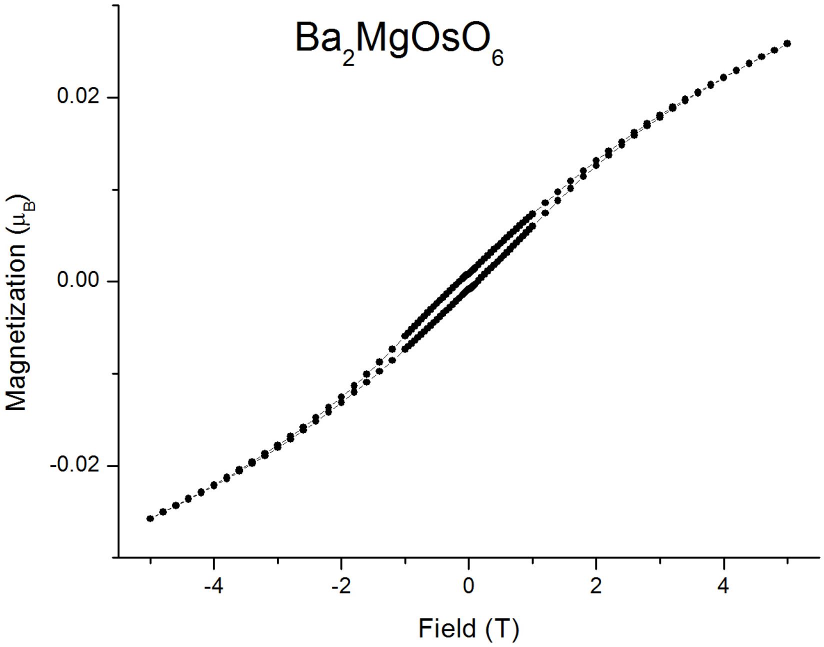

Figure 3.24: Magnetic hysteresis measurements of Ba_2MgOsO_6 at 2K

The magnetic hysteresis measurements on Ba_2MgOsO_6 show small amounts of coercivity from the impurity phase and no saturation.

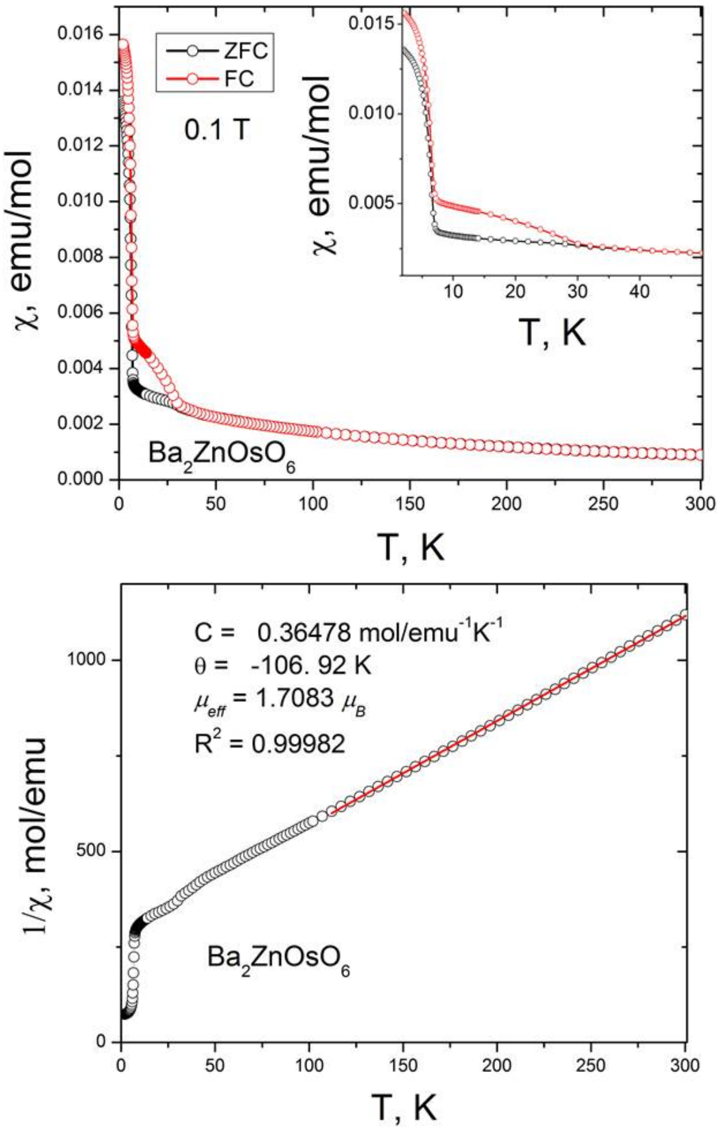

Figure 3.25: On top: ZFC(shown in black) and FC(shown in red) magnetic susceptibility measurements on Ba_2ZnOsO_6. On bottom: Inverse susceptibility of the ZFC data for Ba_2ZnOsO_6

Magnetic susceptibility measurements on Ba_2ZnOsO_6 shows a ZFC/FC divergence and potentially ordered state at ∼30 K with antiferromagnetic interactions (Figure 3.25). Using a Curie-Weiss fit in the high temperature linear region in the inverse susceptibility data gives the following values: C=0.365(5)emu-

K/mole, θ_c=-107(2)K, and $\mu_{eff} = 1.7\mu_B$.

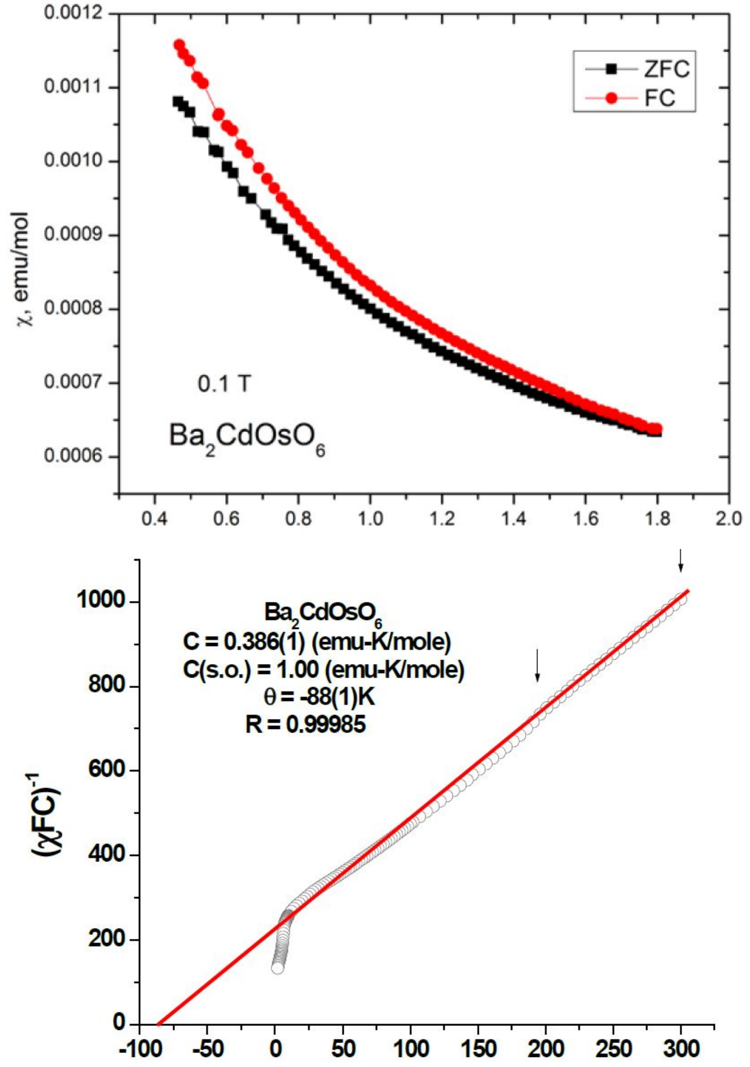

Figure 3.26: On top: ZFC(shown in black) and FC(shown in red) magnetic susceptibility measurements on Ba_2CdOsO_6. On bottom: Inverse susceptibility of the ZFC data for Ba_2CdOsO_6

Magnetic susceptibility measurements on Ba_2CdOsO_6 show no signs of long range order (Figure 3.26). Using a Curie-Weiss fit in the high temperature linear region in the inverse susceptibility data gives the following values:C=0.387(1)emu-

K/mole, θ_c=-88(1)K, and $\mu_{eff} = 1.8\mu_B$.

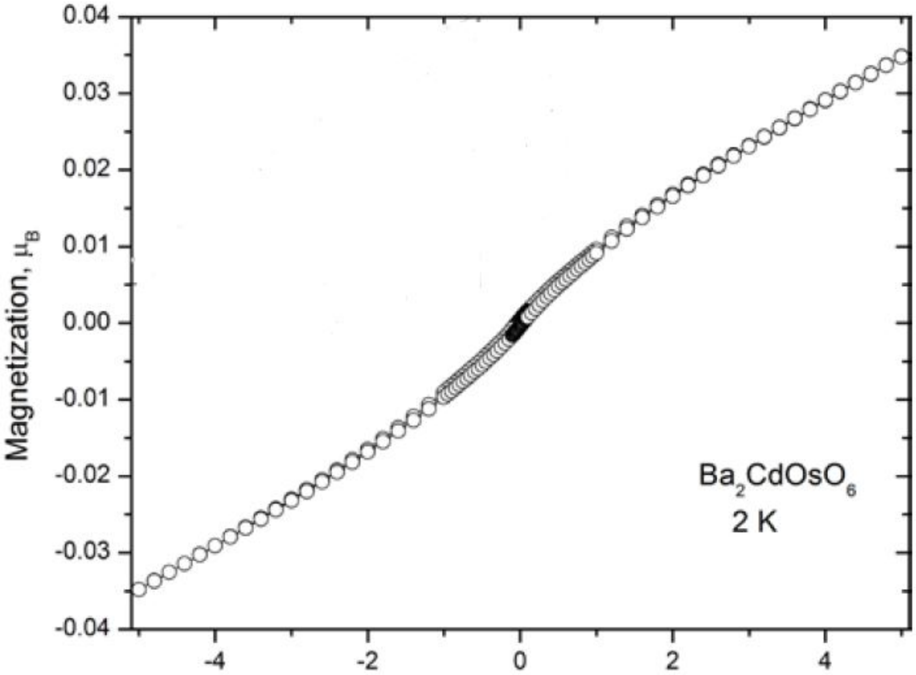

Figure 3.27: Magnetic hysteresis measurements of Ba_2CdOsO_6 at 2K

The magnetic hysteresis measurements on Ba_2CdOsO_6 show small amounts of coercivity from the impurity phase and no saturation (Figure 3.27).

Heat capacity measurements were taken over the range of 4K to 100K and compared to the isostructural non-magnetic tungsten compounds. The heat capacity of the isostructural compounds are fit using three parameters (K_1,K_2,K_3)in the form: C_p=$K_1T+K_2T^3+K_3T^5$. These fits can then be used to subtract an approximation of the non-magnetic contributions to the heat capacity so that only the magnetic portion remains. In comparison to the Ba_2MReO_6 series, the tungsten compounds do not match the magnetic

Ba_2GOsO_6 as well so fewer conclusions can be drawn (Figure 3.28,Figure 3.29, Figure 3.30).

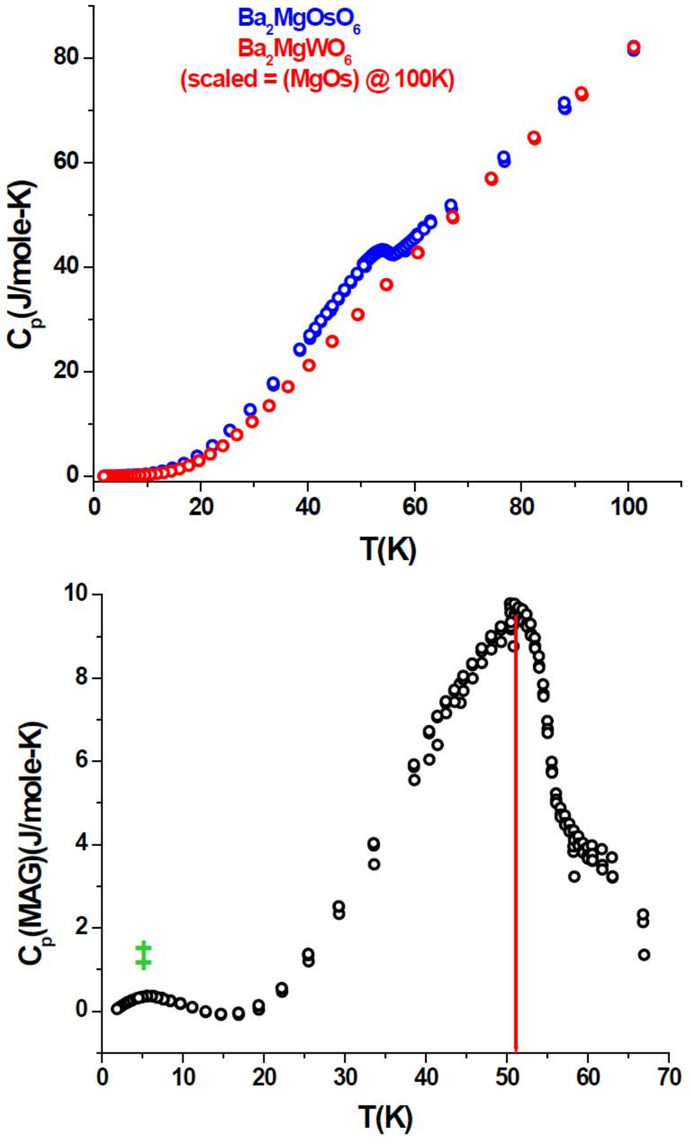

Figure 3.28: On top: Heat capacity of Ba_2MgOsO_6 (shown in blue) and Ba_2MgWO_6 (shown in red. On bottom: Subtraction of the Ba_2MgWO_6 fit to show the magnetic heat capacity of Ba_2MgOsO_6

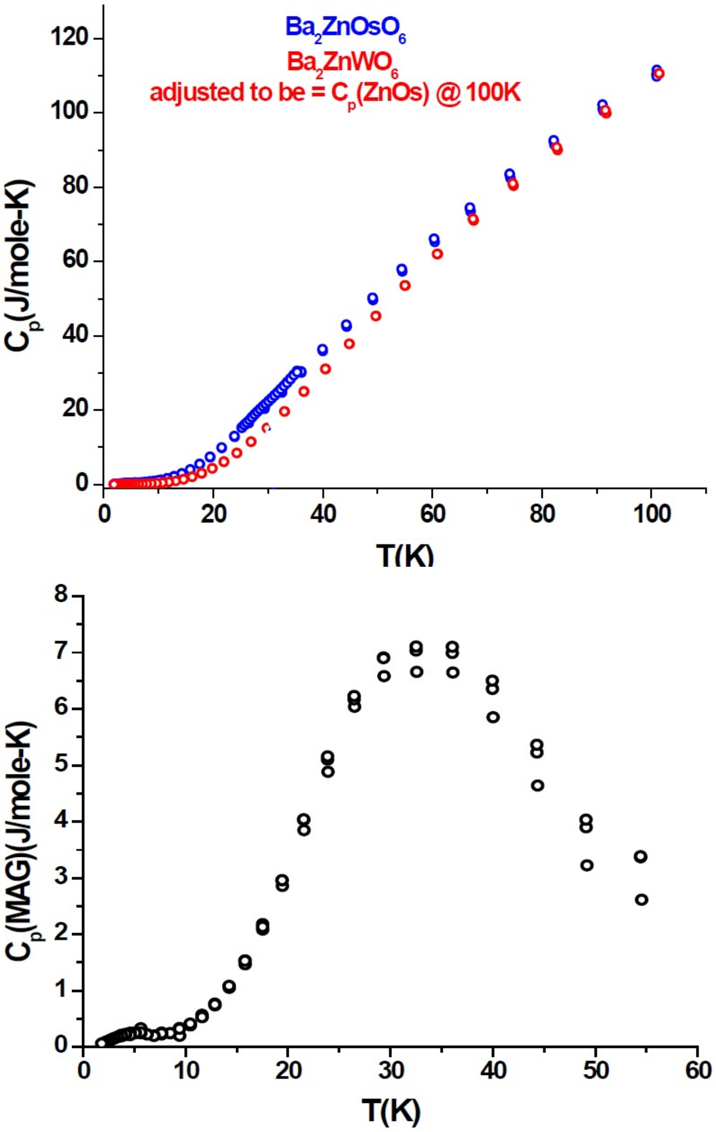

Figure 3.29: On top: Heat capacity of Ba_2ZnOsO_6 (shown in blue) and Ba_2ZnWO_6 (shown in red. On bottom: Subtraction of the Ba_2ZnWO_6 fit to show the magnetic heat capacity of Ba_2ZnOsO_6

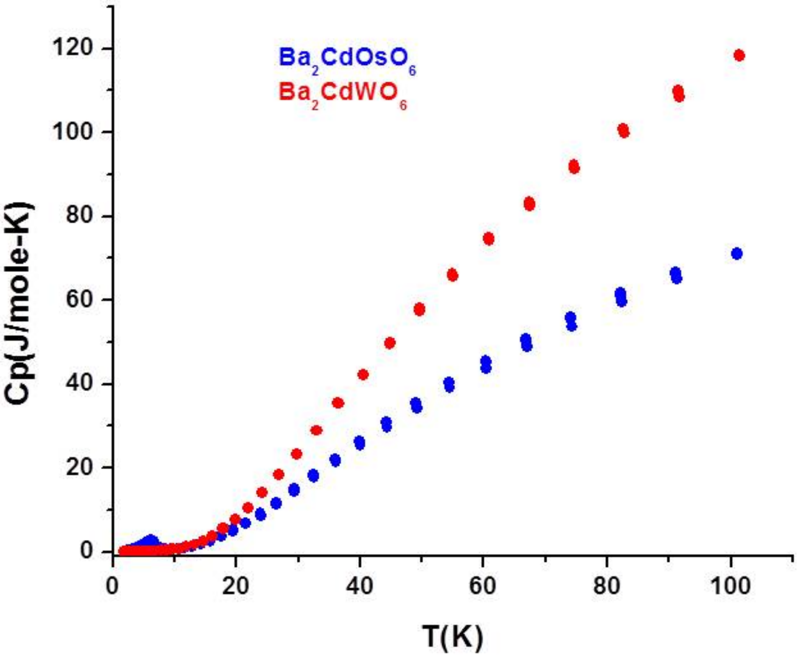

Figure 3.30: Heat capacity of Ba$_2$CdOsO$_6$ (shown in blue) and Ba$_2$CdWO$_6$ (shown in red.

Neutron scattering measurements were also performed at the Spallation Neutron Source (SNS, Oak Ridge National Laboratory), on the SEQUOIA Fine Resolution Fermi Chopper Spectrometer by Dalini Maharaj and Gabriele Sala [16]. For collection of the inelastic scattering data, an incident energy of 40meV and 60meV were used for Ba_2ZnOsO_6 with 60meV and 90meV for Ba_2MgOsO_6. The samples were enclosed in aluminum cells with a He exchange gas atmosphere, loaded into an Orange 4He-flow cryostat, and investigated over a temperature range of 7K to 200K. An identical empty can was measured under the same experimental conditions and used for background subtraction. Ba_2ZnOsO_6 exhibited a spin gap in the low Q region with a gap energy of $\sim$7meV and Ba_2MgOsO_6 also displays a spin gap in the low Q region but with a larger spin gap energy of $\sim$12meV (Figure 3.31 and Figure 3.32).

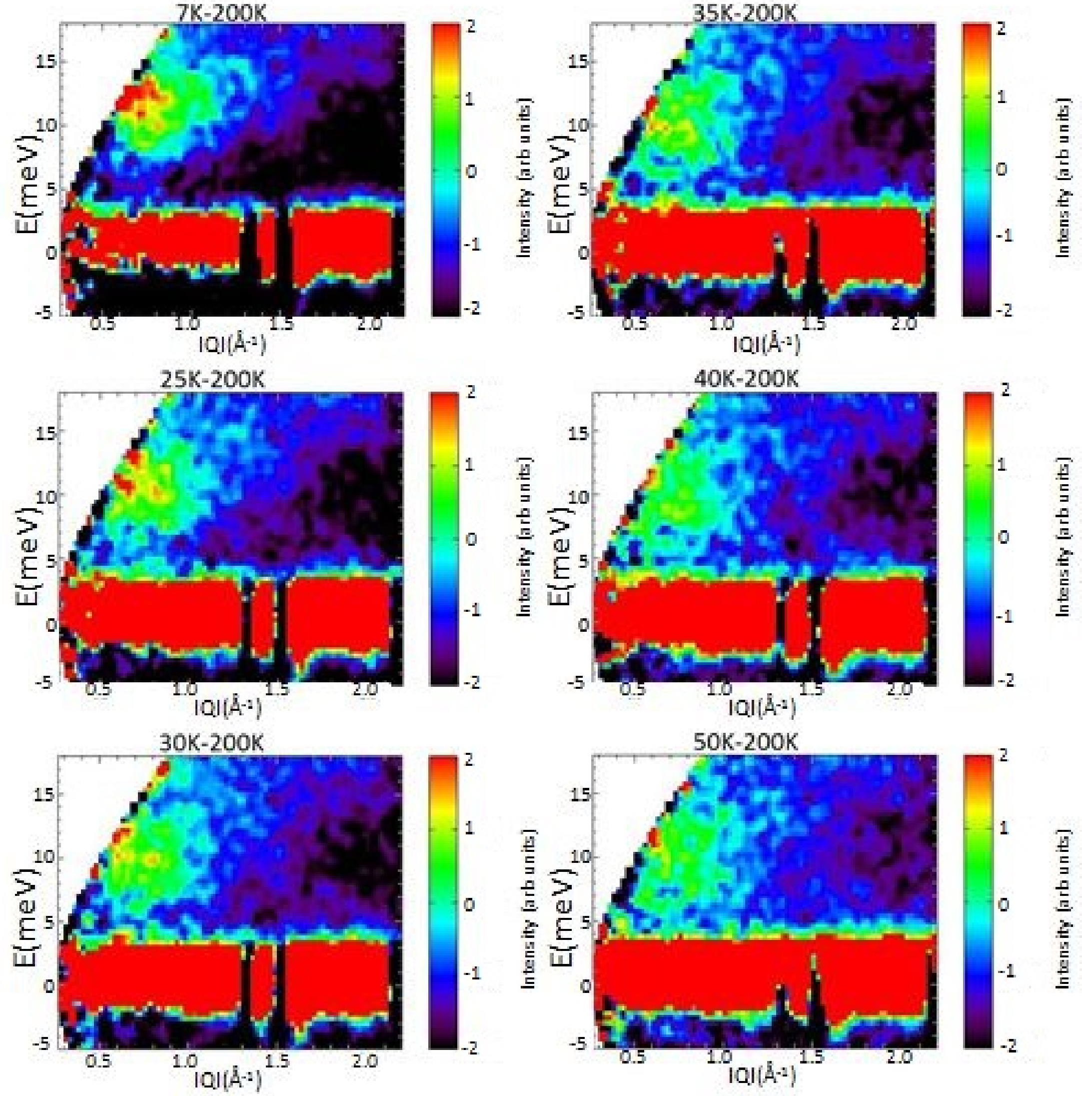

Figure 3.31: 60meV inelastic neutron scattering of Ba_2ZnOsO_6 with a 200K data set used for a background subtraction showing the formation of the spin gap at 7meV.

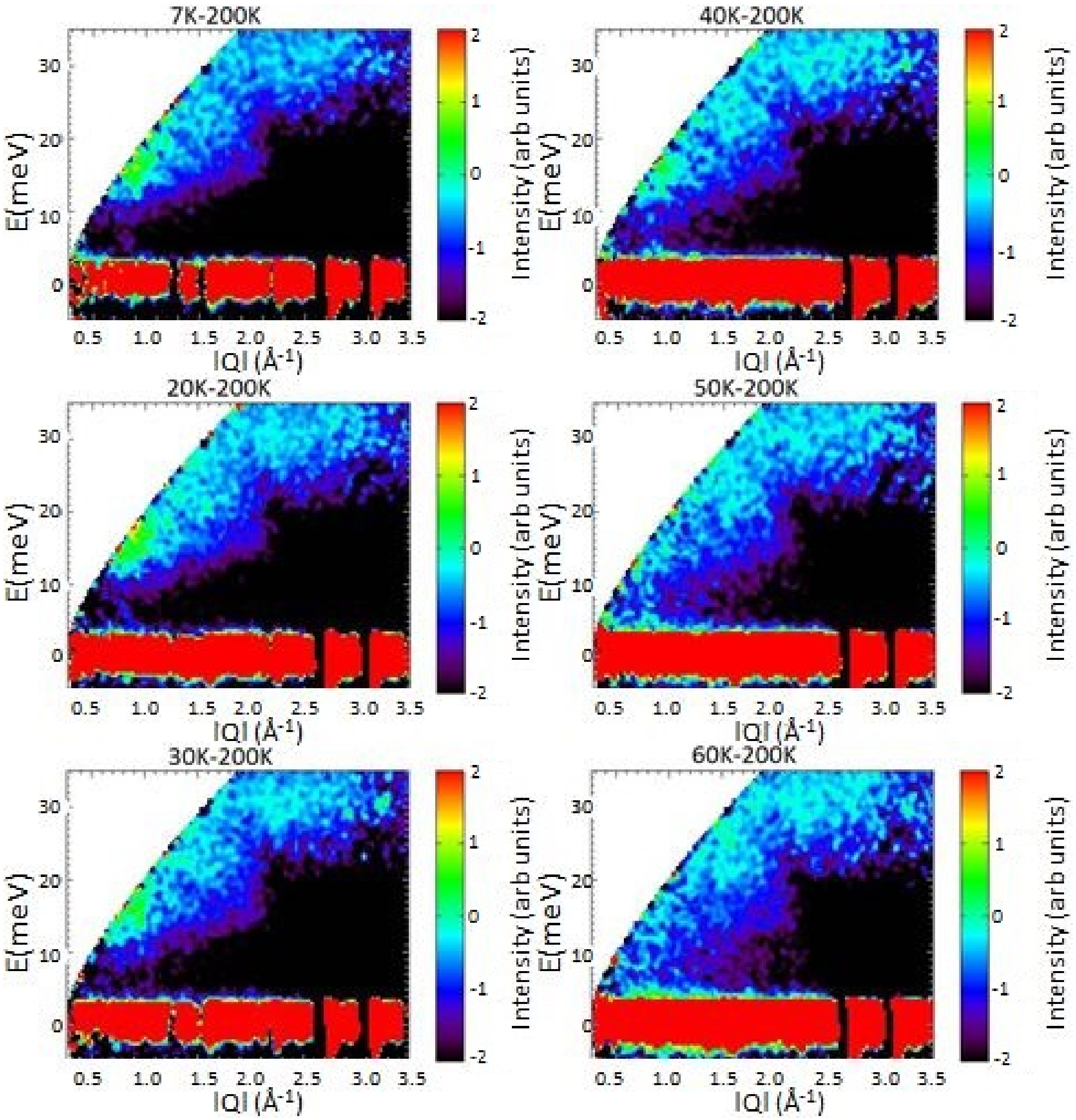

Figure 3.32: 60meV inelastic neutron scattering of Ba_2MgOsO_6 showing the formation of the spin gap at 12meV.

3.4 La_2LiJO_6 where J=(Ru,Os)

La_2LiOsO_6 was prepared using a conventional solid state reaction. A mixture of La_2O_3, 10% excess of Li_2CO_3 and 10% of Os were ground together and heated in air for two hours at 900^{o}C with one intermittent regrinding. For La_2LiRuO_6, a mixture of of La_2O_3, 10% excess of Li_2CO_3, and RuO_2 were ground together and heated in air for one day at 900^{o}C with one intermittent regrinding. Excess of Li_2CO_3 and Os were used to compensate for evaporation. The oxidation state of ruthenium and osmium in these compounds are 5+ which corresponds to an electronic configuration of $4d^3$ and $5d^3$ respectively.

The La_2LiJO_6 series where J=(Ru,Os) form in the monoclinic $P2_1/n$ space group. X-ray powder diffraction data were collected using a PANAlytical X-pert diffractometer using $Cu_{K\alpha1}$ radiation ($\lambda = 1.54056\mathring{A}$) at ambient temperature for all samples over the range 10^o to 120^o in 2θ. This data was then imported into the FullProf Suite and the Rietveld[11] software was used to create fits to the powder x-ray data to extract the lattice parameters for these compounds. Shown in Figure 3.33 is a representative Rietveld fit where the data is shown in red, the black curve is the fit, the blue ticks are expected locations for Bragg peaks, and the blue is the difference between the data and the fit.

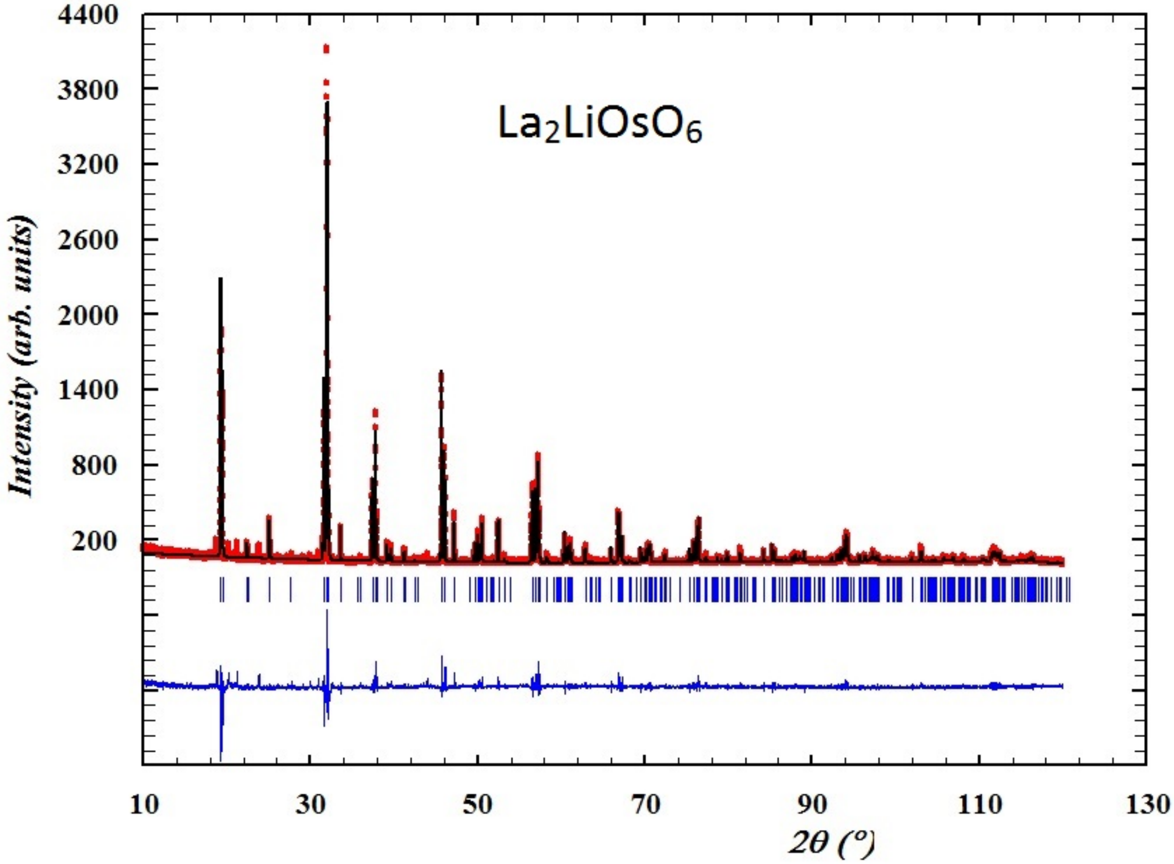

Figure 3.33: Rietveld refinement of La_2LiOsO_6 at room temperature where the data is shown with red dots, the fit is the black line, the blue ticks indicate predicted structural peaks, and the blue line shows the difference between the data and the fit.

The room temperature lattice parameters for La_2LiRuO_6 are a=5.5529(2)$\mathring{A}$, b=5.6010(2)$\mathring{A}$, c=7.8414(3)$\mathring{A}$, and β=90.038(5). For La_2LiOsO_6, the lattice parameters are a=5.56091(5)$\mathring{A}$, b=5.65742(5)$\mathring{A}$, c=7.86884(6)$\mathring{A}$, and β=90.1503(6).

For La_2LiJO_6 (where J=Ru,Os), zero field cooled (ZFC) and field cooled (FC) magnetic susceptibility measurements were performed using a SQUID magnetometer with an applied field of 0.05 T.

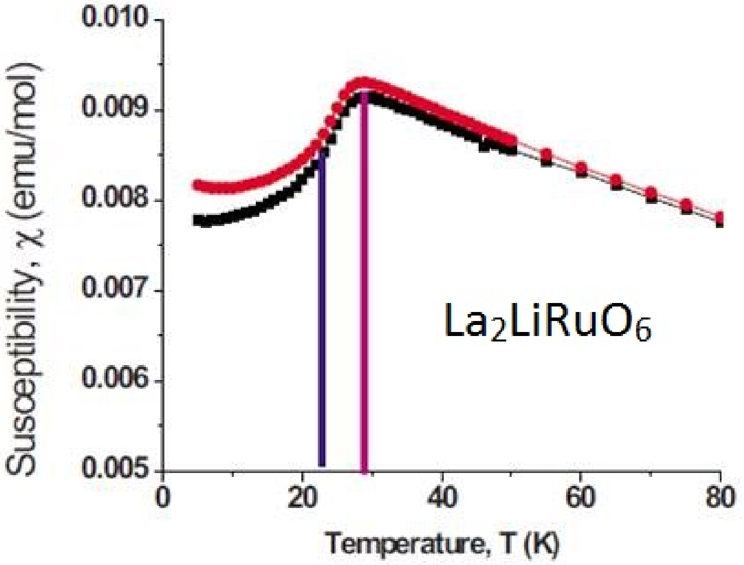

Figure 3.34: ZFC (shown in black) and FC (shown in red) magnetic susceptibility measurements on La_2LiRuO_6

Magnetic susceptibility measurements on La_2LiRuO_6 shown in Figure 3.34 a magnetic phase transition to an antiferromagnetic ordered state at $\sim$ 24K[?]. No divergence between the FC and ZFC data is observed. Using a Curie-Weiss fit in the high temperature linear region in the inverse susceptibility data gives the following values: C=1.93(5) emu-K/mole, θ_c=-185(5)K, and $\mu_{eff} = 3.93(2)\mu_B$.

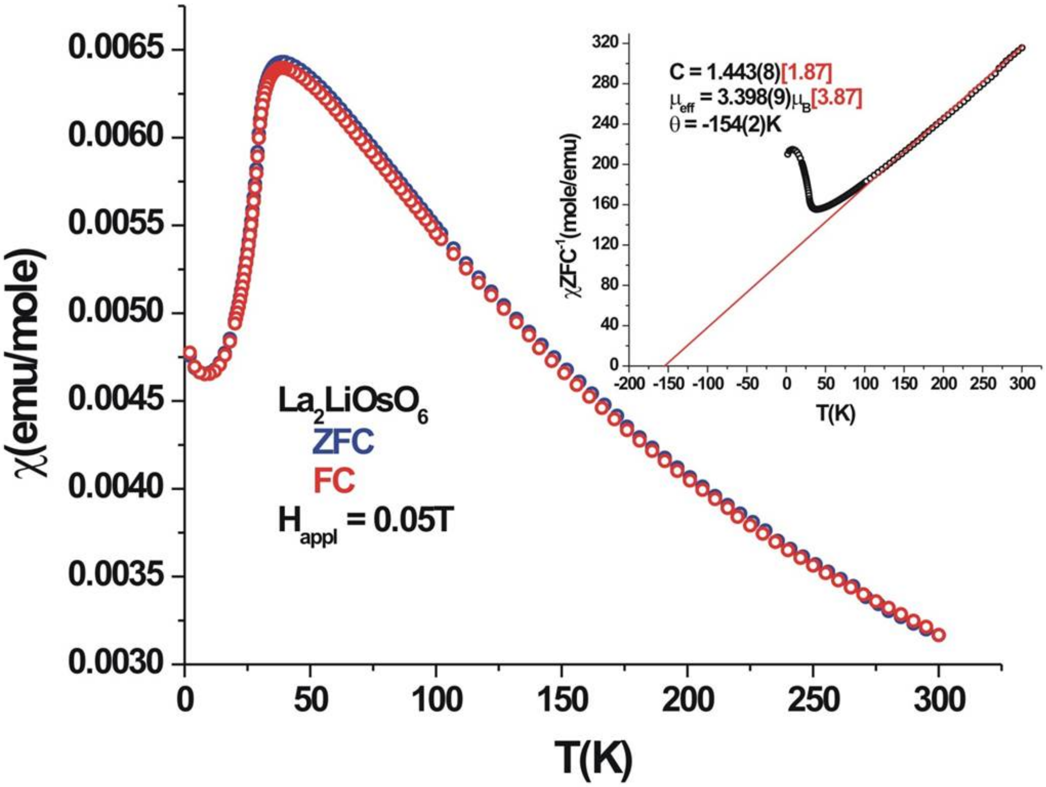

Figure 3.35: ZFC(shown in blue) and FC(shown in red) magnetic susceptibility measurements on La_2LiOsO_6. Inset: Inverse susceptibility of the ZFC data for La_2LiOsO_6

Magnetic susceptibility measurements on La_2LiOsO_6 shown in Figure 3.35 a magnetic phase transition to an antiferromagnetic ordered state at $\sim$ 35K. No divergence between the FC and ZFC data is observed. Using a Curie-Weiss fit in the high temperature linear region in the inverse susceptibility data gives the following values: C=1.443(8) emu-K/mole, θ_c=-154(2)K, and $\mu_{eff} = 3.40(1)\mu_B$.

Neutron diffraction data without energy analysis were collected at the C2 instrument at the NRU reactor operated by the Canadian Nuclear Laboratory, Chalk River, Ontario, Canada. The data were collected at several temperatures from 3.5K to 280K with neutron wavelengths of 2.3719 and/or 1.3305 depending on measurement temperature. The crystal and magnetic structures were refined using the FULLPROF suite of programs[22]. In previous work the Ru^{5+} in La_2LiRuO_6 was determined to have an ordered moment of $2.2(2)\mu_B$ [4] with ordering wave vector (000) as shown in Figure 3.36. La_2LiOsO_6 was found to have an ordered moment of $1.81(4)(6)\mu_B$ with ordering wave vector (1/2 1/2 0) depicted in Figure 3.37 and Figure 3.38. As one would expect from a less than half filled outer shell, the moment on the Os^{5+} ion is smaller than the moment on the Ru^{5+} ion due to spin-orbit coupling.

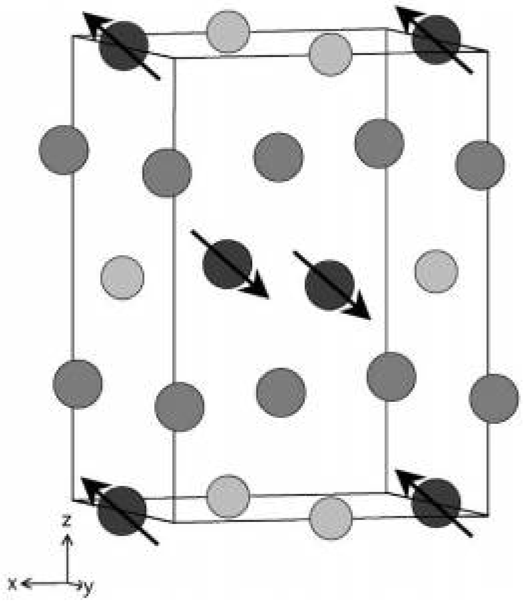

Figure 3.36: Magnetic structure of La_2LiRuO_6 from Rietveld refinement with ordering wave vector k(000)[4].

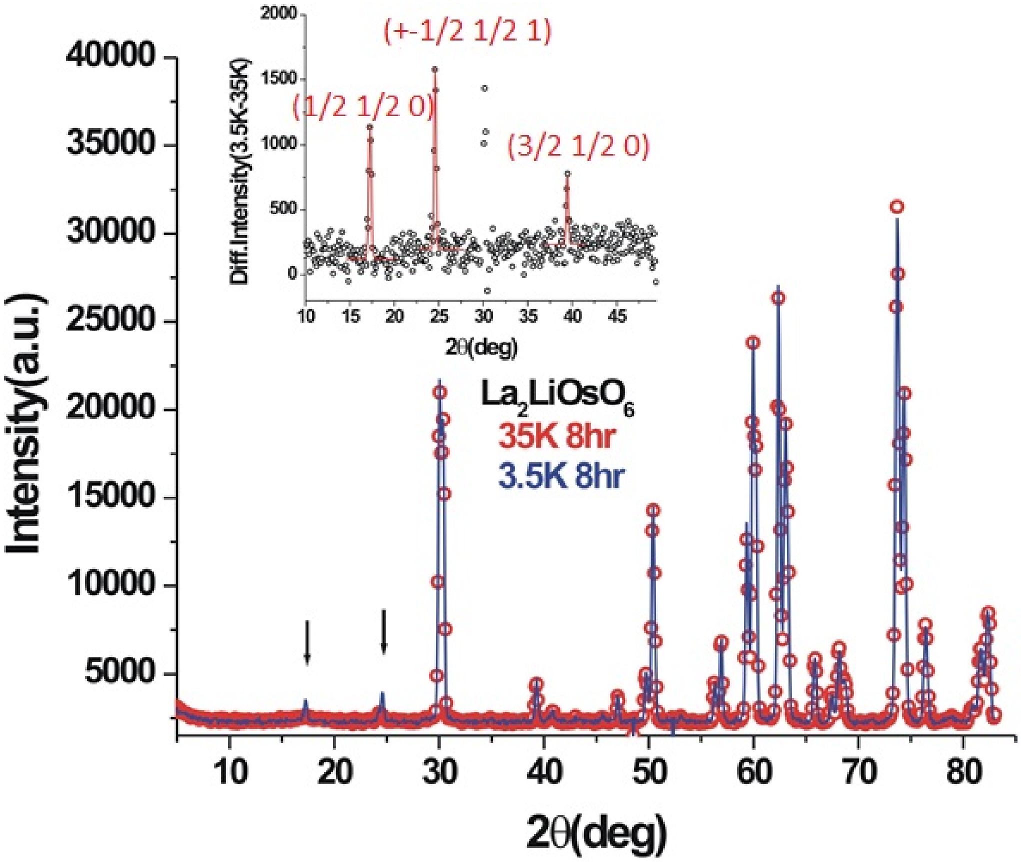

Figure 3.37: Rietveld refinement on elastic neutron diffraction La_2LiOsO_6 at 3.5K for both the nuclear and magnetic structure.

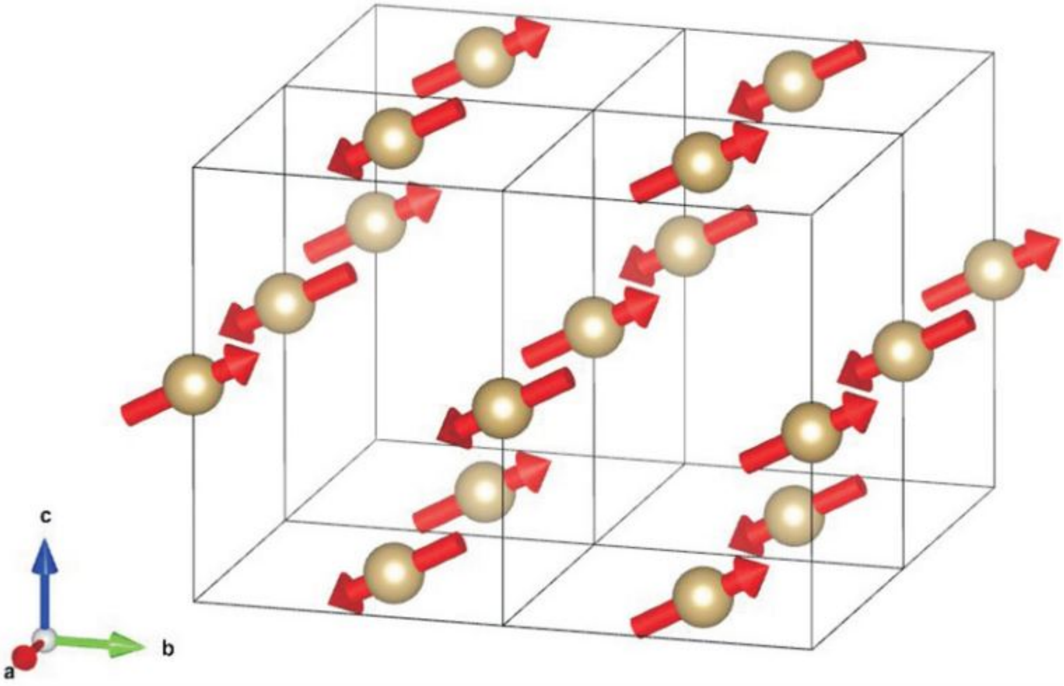

Figure 3.38: Magnetic structure of La_2LiOsO_6 from Rietveld refinement with ordering wave vector k(1/2,1/2,0).

Neutron scattering measurements were also performed at the Spallation Neutron Source (SNS, Oak Ridge National Laboratory), on the SEQUOIA Fine Resolution Fermi Chopper Spectrometer [23]. For collection of elastic scattering data, an incident energy of 11meV was used with an energy integration range from -0.15 to 0.15 meV. The samples were enclosed in annular aluminum cells with a He exchange gas atmosphere, loaded into an Orange 4He-flow cryostat, and investigated over a temperature range of 7K to 100K. An identical empty can was measured under the same experimental conditions and used for background subtraction. La_2LiRuO_6 exhibited a spin gap in the low q region with a gap energy of ∼2.2meV and La_2LiOsO_6 also displays a spin gap in the low q region but with a much larger spin gap energy of ∼7meV (Figure 3.39 and Figure 3.40).

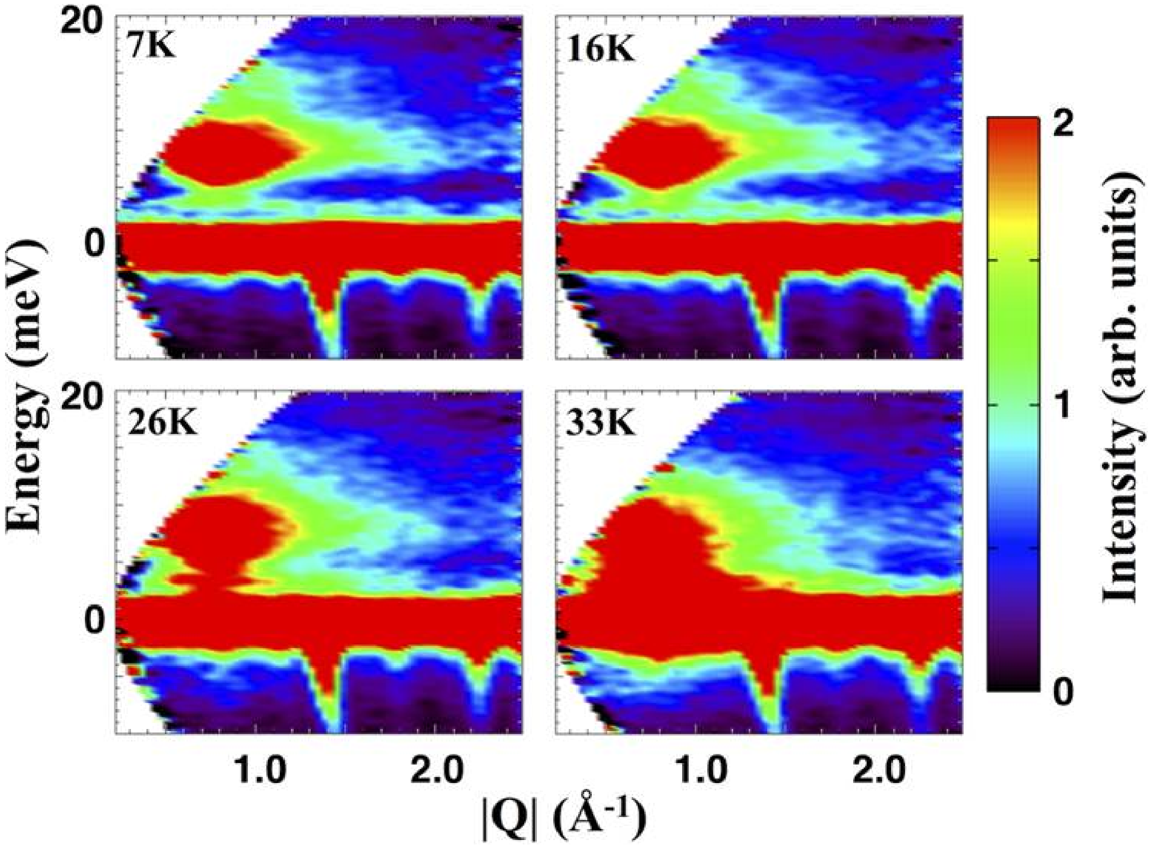

Figure 3.39: Inelastic neutron scattering of La_2LiRuO_6 showing the formation of the spin gap at 2.2meV.

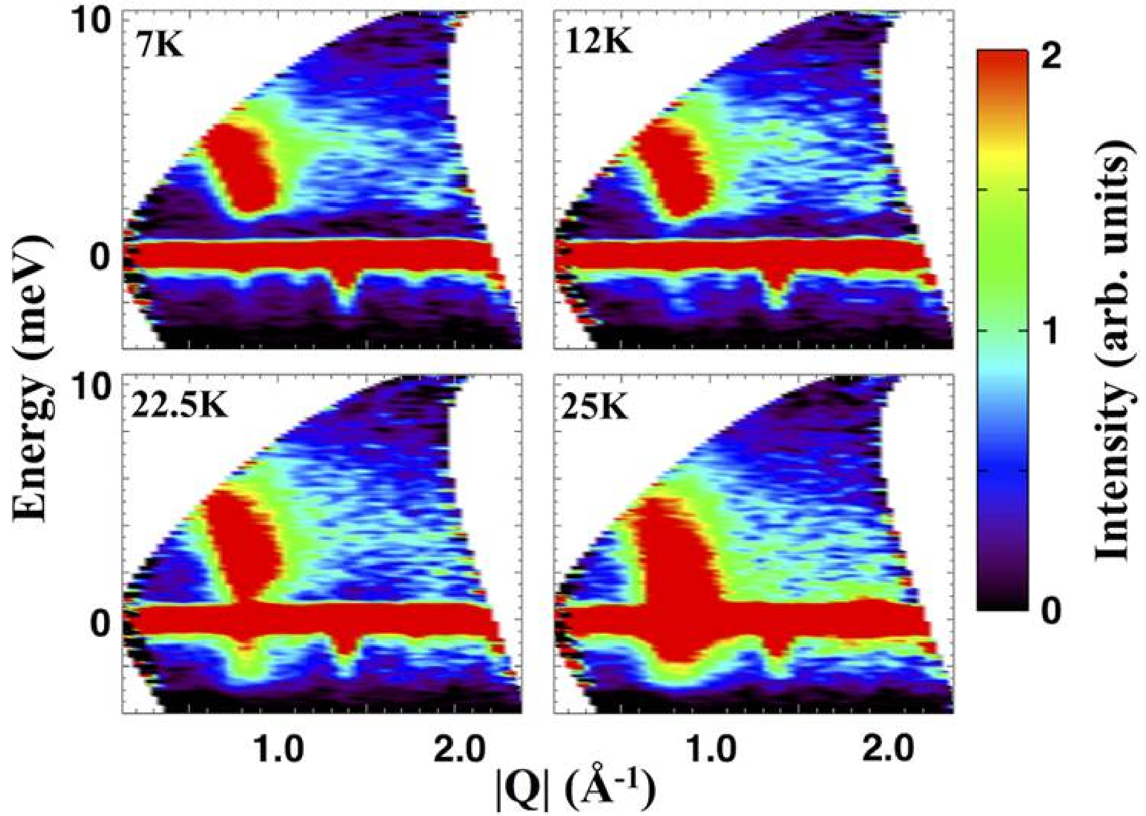

Figure 3.40: Inelastic neutron scattering of La_2LiOsO_6 showing the formation of the spin gap at 7meV.

Chapter 4

Discussion and Conclusion

This investigation seeks to observe trends in the structural and magnetic properties of the double perovskites Ba_2YRuO_6, Ba_2YReO_6,Ba_2YOsO_6, Ba_2MgReO_6, Ba_2ZnReO_6, $Ba_2Y_{2/3}ReO_6$, Ba_2MgOsO_6, Ba_2ZnOsO_6, Ba_2CdOsO_6, La_2LiRuO_6, and La_2LiOsO_6. All of these compounds contain only one magnetic ion with a valence electron configuration of $4d^3$, $5d^1$, $5d^2$, or $5d^3$ depending on the compound. From the ionic radii[5], a tolerance factor was calculated for each double perovskite. Double perovskites with a tolerance factor close to unity were found to form in the cubic space group Fm-3m whereas those with lower tolerance factors formed in the monoclinic space group $P2_1/n$. Lattice parameters for all the investigated double perovskites were determined using a Rietveld refinement on the powder x-ray diffraction data. Table 4.1 includes a summary of the electron configuration, space group, lattice parameters, tolerance factor and references to previous literature. In the cases where previous literature data was available, the results are consistent.

Compound	Electron Configuration	Space Group	Lattice Parameters($\mathring{A}$)	Tolerance Factor	Reference
Ba_2YRuO_6	$4d^3$	Fm-3m	8.3376(4)	0.995	this work
Ba_2YRuO_6	$4d^3$	Fm-3m	8.33559(9)	0.995	[1]
Ba_2YReO_6	$5d^2$	Fm-3m	8.3986(3)	0.992	this work
Ba_2YReO_6	$5d^2$	Fm-3m	8.36278(2)	0.992	[20]
Ba_2YOsO_6	$5d^3$	Fm-3m	8.3560(1)	0.993	this work
Ba_2YOsO_6	$5d^3$	Fm-3m	8.35(7)	0.993	[21]
Ba_2MgReO_6	$5d^1$	Fm-3m	8.0849(2)	1.043	this work
Ba_2MgReO_6	$5d^1$	Fm-3m	8.082	1.043	[22]
Ba_2ZnReO_6	$5d^1$	Fm-3m	8.1148(1)	1.038	this work
Ba_2ZnRe_6	$5d^1$	Fm-3m	8.106	1.038	[22]
$Ba_2Y_{2/3}ReO_6$	$5d^1$	Fm-3m	8.10313(6)	1.074	this work
Ba_2MgOsO_6	$5d^2$	Fm-3m	8.0757(1)	1.044	this work
Ba_2MgOsO_6	$5d^2$	Fm-3m	8.08	1.044	[22]
Ba_2ZnOsO_6	$5d^2$	Fm-3m	8.0975(1)	1.039	this work
Ba_2ZnOsO_6	$5d^2$	Fm-3m	8.095	1.039	[22]
Ba_2CdOsO_6	$5d^2$	Fm-3m	8.3190(1)	0.988	this work
Ba_2CdOsO_6	$5d^2$	Fm-3m	8.362	0.988	[22]
La_2LiRuO_6	$4d^3$	$P2_1/n$	a=5.5529(2) b=5.6010(2) c=7.8414(3) β=90.038(5)	0.944	this work
La_2LiRuO_6	$4d^3$	$P2_1/n$	a=5.5555(2) b=5.5977(2) c=7.8454(3) β=90.020(5)	0.944	[4]
La_2LiOsO_6	$5d^3$	$P2_1/n$	a=5.56091(5) b=5.65742(5) c=7.86884(6) β=90.1503(6)	0.942	this work
La_2LiOsO_6	$5d^3$	$P2_1/n$	a=5.5603(2) b=5.6564(2) c=7.8662(2) β=90.1470(10)	0.942	[9]

Table 4.1: Comparison of structural information between the double perovskites synthesized in this investigation and previous literature. The tolerance factor was calculated using radii from [5]

Magnetic susceptibility measurements were performed with a SQUID magnetometer on all the double perovskites down to 2K. This data was analyzed by plotting the inverse magnetic susceptibilty and using a Curie-Weiss Law fit in the linear high temperature region. However, it is likely that most of these compounds do not have a true Curie-Weiss regime at room temperature and would require higher temperature measurements to have more accurate θ_C constants and effective moments. For example, the curvature near the transition temperatures in Ba_2YRuO_6 and Ba_2YOsO_6 suggest that there are 2D short range correlations which would be non-trivial at room temperature. The approximate θ_C constants and ordering temperatures in these compounds can still give us qualitative information on the degree of magnetic geometric frustration. Elastic neutron experiments were used to determine the ordering wave vectors in compounds with long range order by using Rietveld refinements to fit the nuclear and magnetic peaks. For compounds that display long range ferromagnetic order, the diffraction conditions for the nuclear and magnetic peaks are the same and can make the contribution from the magnetic ordering difficult to resolve. This is the case for the $5d^1$ compounds Ba_2MgReO_6 and Ba_2ZnReO_6 which already have small scattering from due to small moments. It is also valuable to look at the high temperature structure versus the low temperature structure to ensure that no structural changes are taking place. To instrument resolution, for all the measured compounds, no structural changes were observed. Time of flight (TOF) inelastic neutron experiments were used to investigate spin gap formation in all of the double perovskites with the exception of Ba_2CdOsO_6 due to the large neutron absorption cross section of Cd. The spin gap formation is characterized by a feature which is fairly localized in both Q and energy in the inelastic neutron spectrum which occurs in the low Q region but does not intersect the elastic channel. Again due to small scattering from the small moments on the $5d^1$ rhenium compounds, no conclusive results about the presence of a spin gap could be obtained. Repeat experiments on these compounds with different sample can geometry and enhanced counting times would improve the ability to verify the existence of a spin gap. Another feature which could have been observed in these inelastic neutron spectrums was a Jahn-Teller distortion. This would have been seen as a Q-independent feature at 7meV corresponding to a distortion on of the Re-O octahedra. This feature was not seen, supporting that these compounds do not undergo any structural changes at low temperature. A summary of the magnetic susceptibilty data, spin gap energy, ground state and a comparison to available literature values can be found in Table 4.2.

The following measurements performed on the $5d^1$ rhenium series and the $5d^2$ osmium series were done to further explore these materials (as they are not well reported in the literature) and to verify conclusions made with the magnetic susceptibility data. Heat capacity measurements were taken to confirm the ordering temperatures found in the magnetic susceptibilty data. These heat capacity measurements were also compared to non-magnetic isostructural series Ba_2MgWO_6, Ba_2ZnWO_6, $Ba_2Y_{2/3}WO_6$, and Ba_2CdWO_6 to give further evidence of a magnetic transition and also to model the lattice contribution to the heat capacity. For the rhenium compounds the tungsten analogues gave a reasonable model to use for the lattice contribution to the heat capacity. For the osmium compounds the divergence between the data sets was too large. Magnetic hysteresis measurements were performed on Ba_2MgReO_6, Ba_2ZnReO_6, $Ba_2Y_{2/3}ReO_6Ba_2MgOsO_6$, Ba_2ZnOsO_6, and Ba_2CdOsO_6 at 2K with a field of -5 to 5 T. Ba_2MgReO_6 and Ba_2ZnReO_6 displayed ferromagnetic behaviour with coercivities of $\sim$0.2 and 0.08 T and saturated moments of $\sim$0.3 and 0.19 μ_B respectively. $Ba_2Y_{2/3}ReO_6$ shows evidence of a spin glass ground state in the magnetic susceptibilty and the magnetic hysteresis showed no coercivity or saturation which is consistent with a spin glass ground state. The osmium compounds all showed no saturation and slight coercivities which can be attributed to small amounts of the ferromagnetic impurity phase.

Compound	θ_C(K), T$_{ord}$(K), f	spin gap(meV)	Ground State	Ref
Ba_2YRuO_6	-402(3),36,11	5	AFM k(001)	this work,[3]
Ba_2YRuO_6	-522, 36, 16	5	AFM k(001)	[1],[3]
Ba_2YReO_6	-398(3),-,-	inconclusive	spin glass	this work
Ba_2YReO_6	-616(7),-,-	-	spin glass	[20]
Ba_2YOsO_6	-772(4),69,11	17	AFM type k(001)	this work
Ba_2MgReO_6	-141(3)/21.1(1), ∼16,9/1.3	inconclusive	FM	this work
Ba_2MgReO_6	-	-	FM	[23]
Ba_2ZnReO_6	20(1),16,1.3	inconclusive	FM	this work
$Ba_2Y_{2/3}ReO_6$	-528(7),-,-	inconclusive	spin glass	this work
Ba_2MgOsO_6	-51(2),45,1	12	-	this work
Ba_2ZnOsO_6	-107(2),30,4	7	-	this work
Ba_2CdOsO_6	-88(2),-,-	-	no LRO	this work
La_2LiRuO_6	-185(5), ∼24,8	2.2	AFM k(000)	this work,[4]
La_2LiRuO_6	-184,24,8	-	AFM k(000)	[4]
La_2LiOsO_6	-154(2),∼35,4	7	AFM k(1/2,1/2,0)	this work
La_2LiOsO_6	-168,39,4	-	AFM	[24]

Table 4.2: f-frustration index$\left| \frac{\theta_C}{T_{ord}} \right|$, AFM-antiferromagnetic, FM-ferromagnetic, LRO-long range order

From Table4.2, there are two sets of double perovskites -cubic: Ba_2YRuO_6, Ba_2YOsO_6, monoclinic: La_2LiRuO_6, La_2LiOsO_6- which can be used to examine the effects of replacing a 4d^3 ion with a 5d^3 ion. For Ba_2YRuO_6 lattice parameter a=8.3376(4)$\mathring{A}$ and for Ba_2YRuO_6 a=8.3560(1)$\mathring{A}$. This corresponds to a change of ∼0.2% in lattice parameter a and ∼0.7% in the unit cell volume. Since the change in unit cell volume is small, chemical pressure is not expected to have a large influence. Similarly, using the lattice parameters in Table4.1, the change in unit cell volume for La_2LiRuO_6 and La_2LiOsO_6 is ∼5%. The main differences between Ru^{5+} and Os^{5+} are the orbital radial extent and the free ion spin-orbit coupling (SOC) constant. For Ru^{5+} and Os^{5+}, the SOC constants(λ) are 55meV and 186meV respectively [2],[25]. The ratio of these SOC constants is $\frac{\lambda(Os)}{\lambda(Ru)}$ ∼3.4 . This can be compared to the ratio of the spin gap energy in the cubic set ($\frac{E_{gap}Ba_2YOsO_6}{E_{gap}Ba_2YRuO_6} = \frac{17meV}{5meV}$=3.4)and the monoclinic set ($\frac{E_{gap}La_2LiOsO_6}{E_{gap}La_2LiRuO_6} = \frac{7meV}{2.2meV}$ ∼3.2). This suggests that the spin gap formation energy may be related to change in spin-orbit coupling and can be observed in a cubic system as well as a monoclinic system. The ordering temperature increases from 36K in Ba_2YRuO_6 to 69K for Ba_2YOsO_6. Since the change in lattice parameters and unit cell volume is small, this increase can be attributed to the larger orbital radial extent of Os^{5+}. There is an increase in ordering temperatures for La_2LiRuO_6 and La_2LiOsO_6 as well from 24K to 35K. Due to larger change in lattice parameters, the effects of the larger orbital radial extent of Os^{5+} could be slightly diminished and thus the change is not as large ($\frac{35K}{24K} \sim 1.5$ versus $\frac{69K}{36K} \sim 1.9$). As expected the frustration indices for the cubic system are larger than for the monoclinic system.

Ba_2MgOsO_6, Ba_2ZnOsO_6, and Ba_2CdOsO_6 are all cubic and have a valence electron configuration of $5d^2$. The lattice parameters are 8.0757(1)$\mathring{A}$,8.0975(1)$\mathring{A}$, and 8.3190(1)4$\mathring{A}$ respectively. The change in lattice parameter and correspondingly the unit cell volume is caused by the increasing ionic radii of the non-magnetic B site. Having the non-magnetic B site vary influences the ordering temperature as follows: Mg-45K,Zn-30K,Cd-no long range order. It also seen to influence the spin gap energy with 12meV for Ba_2MgOsO_6 and 7meV for Ba_2ZnOsO_6. The lattice parameter and unit cell volume differences between Ba_2MgOsO_6 and Ba_2MgOsO_6 are $\sim 0.3\%$ and $\sim 0.8\%$. Therefore the changes in ordering temperature and spin gap formation are not likely due to chemical pressure but could be influenced by the superexchange pathways through the non-magnetic site.

Bibliography

[1] John E.; Ning Fanlong; Imai Takashi; Michaelis Vladimir; Kroeker Scott; Zhou Haidong; Wiebe Chris R.; Cranswick Lachlan M. D. Aharen, Tomoko; Greedan. *Physical Review B*, 80, 2009.

[2] C. M. Thompson D. D. Maharaj K. Levin S. Kroeker G. E. Granroth R. Flacau Z. Yamani J. E. Greedan E. Kermarrec, C. A. Marjerrison and B. D. Gaulin. The frustrated FCC antiferromagnet Ba2YOsO6: structural characterization, magnetic properties and neutron scattering studies. *Physical Review B*, 91:075133, 2015.

[3] J. P.; Fritsch K.; Marjerrison C. A.; Granroth G. E.; Greedan J. E.; Dabkowska H. A.; Gaulin B. D. Carlo, J. P.; Clancy. *Physical Review B*, 88(2), 2013.

[4] C.P.; Hervieu M.; Martin C.; Moore C.A.; Paik Youn-Kee Battle, P.D.; Grey. *Journal of Solid State Chemistry*, 175:20–26, 2003.

[5] R.D Shannon. *Acta. Cryst A*, 32:751, 1976.

[6] J.E. Greedan. Magnetic Oxides. In R.B. King, editor, *encyclopedia of inorganic chemistry*. Wiley, 1994.

[7] N.W. Ashcroft and N.D. Mermin. *Solid State Physics*. Saunders College, Philadelphia, 1976.

[8] M.T. Anderson et al. *Progress in Solid State Chemistry*, 22:197, 1993.

[9] M.D.; zur Loye H.C. Gemmill, W.R.; Smith. *Journal of Solid State Chemistry*, 179:1750–1756, 2006.

[10] Charles Kittel. Introduction to Solid State Physics. John Wiley & Sons, Inc., New York, 7th edition, 1986.

[11] Juan R. Carvajal. Fullprof: A program for rietveld refinement and pattern matching analysis abstracts of the satellite meeting on powder diffraction of the xv congress of the iucr. 1990.

[12] J. Clarke and A.I. Braginski. Vol.1 Fundamentals and Technology of SQUIDs and SQUID system. In *The SQUID handbook*. Wiley-Vch, Darmstadt, 2004.

[13] D. Pomaranski and J. Kycia. Low Temperature Specific Heat Measurements of Frustrated Magnetic Materials. *Physics in Canada*, 68(2), 2012.

[14] J. et al Beringer. Review of particle physics. *Phys. Rev. D*, 86:010001, Jul 2012.

[15] Roxana Flacau. Probing Materials for Science and Industry, Canadian Neutron Beam Centre neutron spectrometers. "http://www.cnl.ca/site/media/Parent/Spectrometers_Eng.pdf".

[16] Sasha Kolesnikov Matthew Stone. Sequioa-fine resolution fermi chopper spectrometer. "https://neutrons.ornl.gov/sites/default/files/06_G00806H_Instrument_17.pdf".

[17] T.E. Sherline G.E. Granroth, A.I. Kolesnikov. SEQUOIA Operations Manual for Users. Oak Ridge National Laboratories, 2012.

[18] E.S.R. Gopal. Specific Heats at Low Temperatures. pages 90,104. Plenum Press, New York, 1966.

[19] Makoto Wakeshima and Yukio Hinatsu. Crystal structure and magnetic ordering of novel perovskite-related barium osmate ba11os4o24. *Solid State Communications*, 136(910):499 – 503, 2005.

[20] John E.; Bridges Craig A.; Aczel Adam A.; Rodriguez-Jose; MacDougall Greg; Luke Graeme M.; Michaelis Vladimir K.; Kroeker Scott; Wiebe Chris R.; et al Aharen, Tomoko; Greedan. *Physical Review B*, 81, 2010.

[21] S. Kemmler-Sack U. Treiber. Compounds of type Ba2BIIIOsVO6. *Zeitschrift fuer Anorganische und Allgemeine Chemie*, 478:223–232, 1981.

[22] John; Ward Roland Sleight, Arthur W.; Longo. *Inorganic Chemistry*, 1:245–250, 1962.

[23] Helmut; Dehn Jakob K.; Fuess Hartmut Bramnik, Kirill G.; Ehrenberg. *Solid State Sciences*, 5(1):235–241, 2003.

[24] Mark D.; Zur Loye Hans-Conrad Gemmill, William R.; Smith. *Journal of Solid State Chemistry*, 179(6):1750–1756, 2006.

[25] C.-G. Ma and M. G. Brik. *J. of Lumin.*, 145:402, 2014.